Analysis of virtual meson production in a (1 + 1)-dimensional scalar field model

Yongwoo Choi[1,*] Ho-Meoyng Choi[2,†] Chueng-Ryong Ji[3,‡] and Yongseok Oh[1,4,§]

[1]*Department of Physics, Kyungpook National University, Daegu 41566, Korea*
[2]*Department of Physics Education, Teachers College, Kyungpook National University, Daegu 41566, Korea*
[3]*Department of Physics, North Carolina State University, Raleigh, North Carolina 27695-8202, USA*
[4]*Asia Pacific Center for Theoretical Physics, Pohang, Gyeongbuk 37673, Korea*

Light-front time-ordered amplitudes are investigated in the virtual scalar meson production process in $(1 + 1)$ dimensions using the scalar field model extended from the conventional Wick-Cutkosky model. There is only one Compton form factor (CFF) in the $(1 + 1)$-dimensional computation of the virtual meson production process, and we compute both the real and imaginary parts of the CFF for the entire kinematic regions of $Q^2 > 0$ and $t < 0$. We then analyze the contribution of each and every light-front time-ordered amplitude to the CFF as a function of Q^2 and t. In particular, we discuss the significance of the "cat's ears" contributions for gauge invariance and the validity of the "handbag dominance" in the formulation of the generalized parton distribution (GPD) function used typically in the analysis of deeply virtual meson production processes. We explicitly derive the GPD from the "handbag" light-front time-ordered amplitudes in the $-t/Q^2 \ll 1$ limit and verify that the integrations of the GPD over the light-front longitudinal momentum fraction for the Dokshitzer-Gribov-Lipatov-Altarelli-Parisi and Efremov-Radyushkin-Brodsky-Lepage regions correspond to the valence and nonvalence contributions of the electromagnetic form factor that we have recently reported [Phys. Rev. D 103, 076002 (2021)]. We also discuss the correspondence of the GPD to the parton distribution function for the analysis of the deep inelastic lepton-hadron scattering process and the utility of the new light-front longitudinal spatial variable $\tilde{z}$.

I. INTRODUCTION

One of the main goals in hadron physics is to understand the properties and structures of hadrons in terms of quarks and gluons. Since the elastic electron scattering from the nucleon unveiled the non-point-like structure of the nucleon [1], the information on the spatial distributions of charge and current inside the nucleon has been obtained from the electromagnetic (EM) form factors. The information on the momentum distributions of quarks and gluons inside nucleons can also be accessed by the parton distribution functions (PDFs) measured through deep inelastic scattering (DIS) processes [2].

Since the DIS with the longitudinally polarized beam and the polarized target proton yielded the surprising result that the quarks and antiquarks inside the proton carry only about 30% of the total spin of the proton [3], one of the key observables to explore the so-called "proton spin puzzle" has been the set of generalized parton distributions (GPDs) [4–12]. GPDs describe internal parton structures of the hadron, unifying the investigation of form factors and PDFs. In particular, the parton's orbital angular momentum contribution to the nucleon spin may be estimated with the formulation of GPDs. The extraction of GPDs from the experimental data can be accessed mainly by hard exclusive electroproduction processes such as the deeply virtual Compton scattering (DVCS) and the deeply virtual meson production (DVMP) processes. In these processes, an electron interacts with a parton from the hadron, e.g., the nucleon, by the exchange of a virtual photon, and the struck parton radiates a real photon (DVCS process) or hadronizes into a meson (DVMP process) [13–18]. Both in DVCS and DVMP, the GPD formalism relies on the "handbag dominance" representing the factorization of the hard and soft parts in the respective scattering amplitudes.

*[*]sunctchoi@gmail.com
[†]homyoung@knu.ac.kr
[‡]ji@ncsu.edu
[§]yohphy@knu.ac.kr

Here, the light-front dynamics (LFD) plays an important role in providing both the skewness ζ and the light-front (LF) longitudinal momentum fraction x of the parton struck by the probing virtual photon off the target. It is well known that the integrals of the leading-twist GPDs in the s- and u-channel handbag amplitudes of both DVCS and DVMP processes carry the factorized denominator factors such as $1/(x - \zeta)$ and $1/x$, respectively.

While the virtual Compton scattering (VCS) process is coherent with the Bethe-Heitler (BH) process [19], the virtual meson production (VMP) process does not possess complications from the involvement of the BH process and offers a unique way for experimental exploration of the hadronic structure for the study of quantum chromodynamics and strong interactions. In particular, the coherent electroproduction of pseudoscalar ($J^{PC} = 0^{-+}$) or scalar (0^{++}) mesons off a scalar target (for example, the ^{4}He nucleus [20]) provides an excellent experimental terrain to discuss the fundamental nature of hadrons without involving much complication from the spin degrees of freedom. In Ref. [21], two of us discussed the most general formulation of the differential cross sections for the meson (0^{-+} or 0^{++}) production processes which involve only one or two hadronic form factors, respectively, when the target is a scalar particle. In particular, the beam spin asymmetry was discussed and our findings from the general formulation were contrasted with respect to the GPD formulation.

In the present article, we investigate the electroproduction process of a scalar meson off a scalar target, simulating for example, $\gamma^* + {}^4\text{He} \to f_0(980) + {}^4\text{He}$, in the one-loop level of the $(1 + 1)$-dimensional scalar field model extended from the conventional Wick-Cutkosky model [22]. The same scalar field model was previously applied to the analysis of the longitudinal charge density [23]. As described in Ref. [23], our model is essentially the $(1 + 1)$-dimensional quantum field theoretic model of Sawicki and Mankiewicz [24,25], which was reinvestigated by several others [26–30]. In this model, the wave function is obtained as the solution of the covariant Bethe-Salpeter (BS) equation in the ladder approximation with a relativistic version of the contact interactions [26]. The covariant model wave function is a product of two free single-particle propagators, the Dirac delta function for the overall momentum conservation, and a constant vertex function. Consequently, all our Compton form factor calculations show various ways of evaluating the Feynman box diagrams in the scalar field model taken in the present work.

As the transverse rotations are absent in $(1 + 1)$ dimensions, the advantage of the LFD with the LF time $x^+ = x^0 + x^3$ as the evolution parameter is maximized in contrast to the usual instant form dynamics (IFD) with the ordinary time x^0 as the evolution parameter. In LFD, the individual x^+-ordered amplitudes contributing to the hadronic form factor are invariant under the boost, i.e., frame independent, while the individual x^0-ordered amplitudes in IFD are not

invariant under the boost but dependent on the reference frame. As only one hadronic form factor is involved in $(1 + 1)$ dimensions for the electroproduction process of a scalar meson off a scalar target, the analysis may be regarded relatively simple without involving the beam spin asymmetry. The extension to the $(3 + 1)$-dimensional analysis involves the transverse rotations not kinematical but dynamical in LFD. One more hadronic form factor involved in the $(3 + 1)$-dimensional analysis would lead to a nonvanishing beam spin asymmetry. As discussed in Ref. [21], the beam spin asymmetry vanishes trivially in the GPD formulation for the scalar meson production off the scalar target unless the chiral-odd GPD is included. This nontrivial aspect of the $(3 + 1)$-dimensional extension deserves a separate further investigation going beyond the scope of the present work. We note however that the $(1 + 1)$-dimensional analysis presented in this work corresponds to the $(3 + 1)$-dimensional analysis in the forward direction, where the GPD formulation is most applicable. In this work, we thus focus on analyzing the essential features of the LFD by benchmarking the $(1 + 1)$-dimensional characteristics of the VMP process.

The extraction of the hadronic form factor, the so-called Compton form factor (CFF), is made by utilizing the general formulation of the hadronic currents presented in Ref. [21]. The real and imaginary parts of the CFF are extracted explicitly. In order to explore the applicability of the handbag dominance adopted in the GPD formulation, we extract the GPD in the DVMP limit and verify that the integrations of the GPD over x for the Dokshitzer-Gribov-Lipatov-Altarelli-Parisi (DGLAP) $(1 > x > \zeta)$ and Efremov-Radyushkin-Brodsky-Lepage (ERBL) $(\zeta > x > 0)$ regions correspond to the respective valence and nonvalence contributions of the electromagnetic form factor that we have recently presented in Ref. [23]. The correspondence of the GPD to the PDF is also discussed with the new LF longitudinal spatial variable $\tilde{z} = x^- p^+$ recently introduced in Ref. [31]. We then contrast the CFF obtained from the GPD formulation with the CFF result from the general formulation of the VMP process in the present scalar field model.

This article is organized as follows. In Sec. II, we present the kinematics of the virtual meson production process off the scalar target. Section III is devoted to the derivation of the exact form of the CFF in the VMP process within the one-loop level of the scalar field model in $(1 + 1)$ dimensions. Complete analyses for various LF time-ordered diagrams involved in the VMP process are presented as well. In Sec. IV, we extract the GPD, PDF, longitudinal probability density (LPD) in the LF coordinate space, and the EM form factor in the DVMP limit. Section V presents our numerical results for the CFF, GPD, PDF, LPD, and EM form factor of the scalar target simulating the mass arrangement of the $\gamma^* + {}^4\text{He} \to f_0(980) + {}^4\text{He}$ process. We summarize and conclude in Sec. VI.

II. KINEMATICS

We begin with the kinematics involved in the virtual-photon scattering off the scalar target ($\mathcal{M}$) for the production of the scalar meson (S),

$$\gamma^*(q) + \mathcal{M}(p) \rightarrow S(q') + \mathcal{M}(p'), \qquad (1)$$

where the initial (final) scalar target state is characterized by the momentum $p(p')$ and the incoming virtual photon and the outgoing meson by q and q', respectively. We shall use the component notation $a = (a^+, a^-)$ in $(1 + 1)$ dimensions and the metric is specified by $a^\pm = a^0 \pm a^3$ and $a \cdot b = (a^+ b^- + a^- b^+)/2$.

Defining the four momentum transfer $\Delta = p - p'$, we have

$$p = \left(p^+, \frac{M_T^2}{p^+} \right),$$

$$p' = \left((1 - \zeta)p^+, \frac{1}{p^+} \left(M_T^2 - \frac{t}{\zeta} \right) \right), \qquad (2)$$

and

$$\Delta = \left(\zeta p^+, \frac{t}{\zeta p^+} \right), \qquad (3)$$

where M_T is the target mass and $\zeta = \Delta^+/p^+$ is the skewness parameter describing the asymmetry in plus momentum. The squared momentum transfer then reads

$$t = \Delta^2 = 2p \cdot \Delta = -\zeta^2 M_T^2/(1 - \zeta) \leq 0, \qquad (4)$$

which defines ζ in terms of t as

$$\zeta = \frac{1}{2M_T^2} \left(t + \sqrt{t^2 - 4tM_T^2} \right), \qquad (5)$$

so that $0 \leq \zeta \leq 1$ is taken. Considering the fact that $q^+ \neq 0$ in $(1 + 1)$ dimensions, we choose the momenta q and q' as

$$q = \left((\mu_s \zeta' - \zeta)p^+, \frac{Q^2}{p^+} \left(\frac{1}{\zeta'} + \frac{\tau}{\zeta} \right) \right),$$

$$q' = \left(\mu_s \zeta' p^+, \frac{Q^2}{\zeta' p^+} \right), \qquad (6)$$

where $\mu_s = M_S^2/Q^2$ and $\tau = -t/Q^2$ with $q^2 = -Q^2$ and M_S being the mass of the produced scalar meson. It also gives the definition of ζ' through the relation with ζ as

$$\frac{\zeta'}{\zeta} = \frac{2}{1 + \mu_s - \tau + \sqrt{(1 + \mu_s + \tau)^2 - 4\tau}}, \qquad (7)$$

where $0 \leq \mu_s \zeta' < \zeta \leq 1$ is taken in deriving Eq. (7) so that $q^+ < 0$. The Bjorken variable $x_{\mathrm{Bj}} = Q^2/(2p \cdot q)$ is then given by

$$x_{\mathrm{Bj}} = \frac{2t}{t(1 + \mu_s + \tau) - \sqrt{t(t - 4M_T^2)[(1 + \mu_s + \tau)^2 - 4\tau]}}. \qquad (8)$$

The maximum value of x_{Bj} for a given value of Q^2 is obtained by the condition that

$$\left. \frac{dx_{\mathrm{Bj}}}{dt} \right|_{t = t_{\mathrm{th}}} = 0, \qquad (9)$$

which determines the threshold momentum transfer squared $t_{\mathrm{th}}(Q^2)$ as

$$t_{\mathrm{th}}(Q^2) = -\frac{M_T(M_S^2 + Q^2)}{M_T + M_S}. \qquad (10)$$

This corresponds to the threshold point where momentum directions of the outgoing target and the produced meson are swapped in the center-of-momentum frame.

In the deeply virtual limit where Q^2 is very large compared to other scales of M_T^2, M_S^2, and $|t|$, one can easily find that $\zeta \simeq x_{\mathrm{Bj}}$; i.e., ζ plays the role of x_{Bj}. We also note that ζ and t are not independent in $(1 + 1)$ dimensions while they are in general independent of each other in $(3 + 1)$ dimensions because of the nonzero transverse component of Δ. Explicitly, we have $t = -(\zeta^2 M_T^2 + \Delta_\perp^2)/(1 - \zeta)$ in $(3 + 1)$ dimensions [12] where $\Delta_\perp^2$ is the transverse momentum transfer squared. Defining the skewness parameters $\zeta = \zeta_{1+1}$ and $\zeta = \zeta_{3+1}$ in $(1 + 1)$ and $(3 + 1)$ dimensions, respectively, one can obtain the allowed range of ζ_{3+1} as $0 \leq \zeta_{3+1} \leq \zeta_{1+1}$ for a fixed value of t. Here, we note that the limit $t \rightarrow 0$ implies $\zeta_{1+1} \rightarrow 0$, while there is no such correlation between $t \rightarrow 0$ and $\zeta_{3+1} \rightarrow 0$ unless $\Delta_\perp^2 \rightarrow 0$ is imposed as well. This indicates that the $(1 + 1)$-dimensional computation simulates only the forward production of the meson in the $(3 + 1)$-dimensional computations as expected intuitively. As shown in Eq. (4), the value of $-t$ is also not independent of the target mass M_T in the $(1 + 1)$-dimensional computations. Thus, for a given $-t$ value, the skewness parameter ζ_{1+1} gets smaller as M_T increases. The consequence of such constraint in $(1 + 1)$ dimensions will be revealed in the comparison of the CFF between the predictions from the GPD formulation deduced in the DVMP limit and our exact VMP computations obtained in the present work. In particular, the condition that $Q^2 \gg M_T^2$ may not be required for the DVMP limit in the $(1 + 1)$-dimensional computations because of the correlation among ζ_{1+1}, t, and M_T^2. This would then imply that the condition $Q^2 \gg M_T^2$ may also not

be required for the forward production of mesons in the $(3+1)$-dimensional computations.

III. MODEL CALCULATIONS FOR VIRTUAL MESON PRODUCTION

In general, the total scattering amplitude $\mathcal{M}_{\text{tot}}^\mu$ for scalar meson production off the scalar target of Eq. (1) is expressed in terms of two independent CFFs [21] as[1]

$$\mathcal{M}_{\text{tot}}^\mu = [(\Delta \cdot q)q^\mu - q^2\Delta^\mu]\mathcal{F}_1 + [(\Delta \cdot q)\mathcal{P}^\mu - (\mathcal{P} \cdot q)\Delta^\mu]\mathcal{F}_2$$
$$\equiv A^\mu \mathcal{F}_1 + B^\mu \mathcal{F}_2, \qquad (11)$$

which defines A^μ and B^μ, where $\mathcal{P} = p + p'$. The EM current conservation in Eq. (11) is assured by the condition $q \cdot \mathcal{M}_{\text{tot}} = 0$. The CFFs are measurable physical quantities and are related to the GPDs in the deeply virtual kinematic region, e.g., $Q^2 \gg -t$. For the VCS process, it is not possible to distinguish whether the emitted real photon comes from the loop process in the hadronic sector or from the scattered electron, i.e., the BH process [19]. However, the VMP does not have a BH-type process since the scalar meson cannot be emitted from the electron.

Furthermore, the two CFFs $\mathcal{F}_1$ and $\mathcal{F}_2$ in Eq. (11) are not linearly independent in $(1+1)$ dimensions since the two covariant vectors A^μ and B^μ are parallel to each other, i.e., $B^\mu = cA^\mu$, where the scaling factor c reads

$$c = 2\sqrt{\frac{t(t - 4M_T^2)}{M_S^4 + 2M_S^2(Q^2 - t) + (Q^2 + t)^2}}, \qquad (12)$$

for $\mu = \pm$. This leads us to redefine $\mathcal{M}_{\text{tot}}^\mu$ in $(1+1)$ dimensions with one CFF as

$$\mathcal{M}_{\text{tot}}^{\mu(1+1)} = [(\Delta \cdot q)q^\mu - q^2\Delta^\mu]\mathcal{F}, \qquad (13)$$

where $\mathcal{F} = \mathcal{F}_1 + c\mathcal{F}_2$.

In the following, we shall perform the LF calculations of $\mathcal{M}_{\text{tot}}^{\mu(1+1)}$ using the model based on the covariant BS calculations of $(1+1)$-dimensional scalar field theory. As the beam spin asymmetry for scalar meson production is absent in $(1+1)$ dimensions because of the singleness of CFF, we do not need to involve the beam helicity but just focus on the LF calculations of the covariant scalar field model. We analyze the detailed structure of scattering amplitude coming from the loop diagrams below.
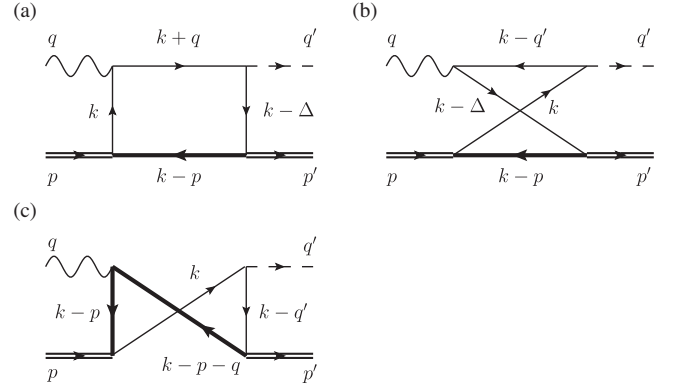
FIG. 1. Relevant Feynman diagrams for the reaction of $\gamma^*(q) + \mathcal{M}(p) \to S(q') + \mathcal{M}(p')$. (a) The s-box diagram, (b) the u-box diagram, and (c) the cat's ears diagram.

A. Amplitudes from loop diagrams

For simplicity, we assume that the scalar target is made up of two scalar constituents, Q_1 and Q_2, with mass and charge (m_{Q_1}, e_{Q_1}) and $(m_{Q_2}, e_{\bar{Q}_2})$, respectively. The Mandelstam variables are defined as $s = (p + q)^2$ and $u = (p - q')^2$. The loop contribution to the scattering amplitude $\mathcal{M}_{\text{tot}}^\mu$ is given by[2]

$$\mathcal{M}_{\text{loop}}^\mu = \mathcal{M}_s^\mu + \mathcal{M}_u^\mu + \mathcal{M}_c^\mu, \qquad (14)$$

where $\mathcal{M}_s^\mu$ and $\mathcal{M}_u^\mu$ are the s- and u-channel amplitudes as shown in Figs. 1(a) and 1(b), respectively. The diagram shown in Fig. 1(c) is the diagram of "cat's ears," which we denote as "c-channel" amplitude. The inclusion of the c-channel amplitude is crucial to satisfy the gauge invariance.

In the solvable covariant BS model of $(1+1)$-dimensional scalar field theory, the scattering amplitudes of the s-, u-, and c-channels in the one-loop approximation are written as

$$\mathcal{M}_s^\mu = ie_{Q_1}\mathcal{N} \int \frac{d^2k}{(2\pi)^2} \frac{(2k+q)^\mu}{N_k N_{k+q} N_{k-\Delta} D_{k-p}},$$

$$\mathcal{M}_u^\mu = ie_{Q_1}\mathcal{N} \int \frac{d^2k}{(2\pi)^2} \frac{(2k-2q'+q)^\mu}{N_k N_{k-q'} N_{k-\Delta} D_{k-p}},$$

$$\mathcal{M}_c^\mu = -ie_{\bar{Q}_2}\mathcal{N} \int \frac{d^2k}{(2\pi)^2} \frac{(2k-2p-q)^\mu}{N_k N_{k-q'} D_{k-p-q} D_{k-p}}, \qquad (15)$$

where the denominators are coming from the intermediate scalar propagators shown in Fig. 1. Here, $N_{p_1} = p_1^2 - m_{Q_1}^2 + i\epsilon$ and $D_{p_2} = p_2^2 - m_{Q_2}^2 + i\epsilon$. The normalization constant $\mathcal{N}$ includes the coupling constants involved in this reaction. The electric charges satisfy the charge

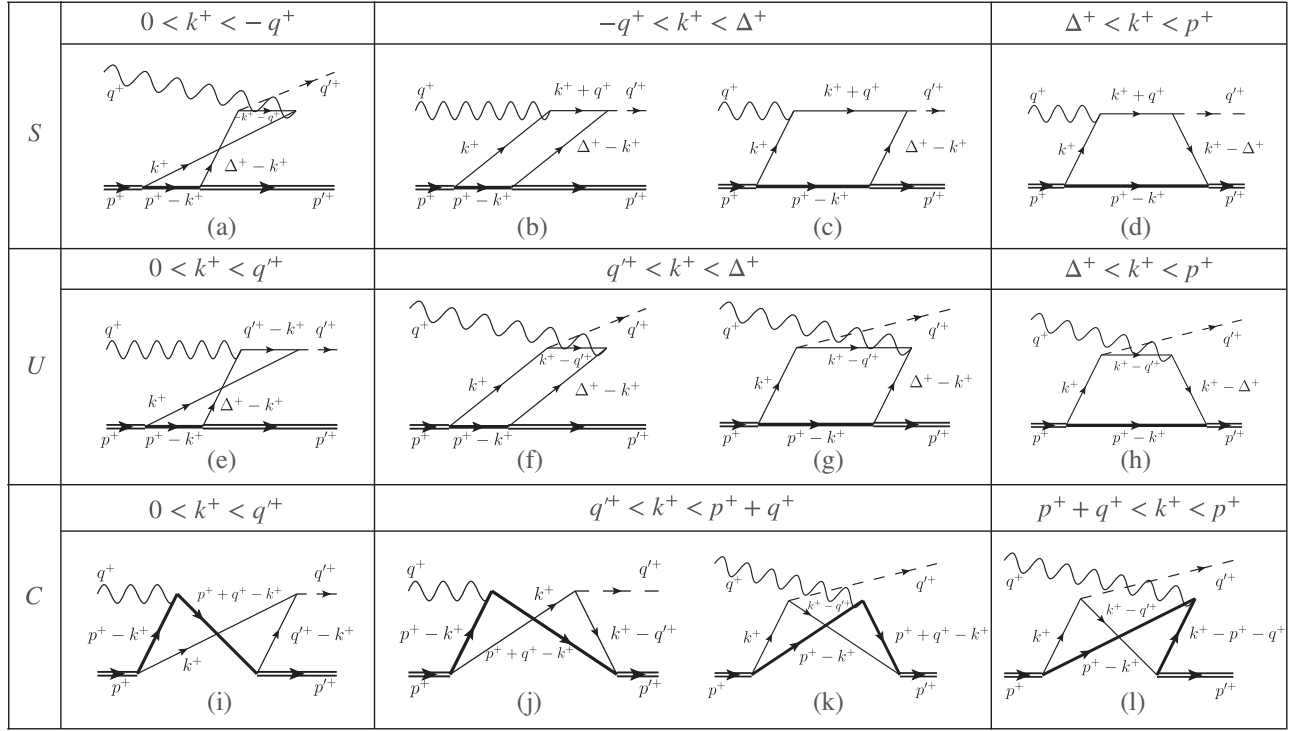FIG. 2. The LF time-ordered diagrams for the scattering amplitudes $(\mathcal{M}_s^\mu, \mathcal{M}_u^\mu, \mathcal{M}_c^\mu)$ corresponding to the (s, u, c)-channels.

conservation, $e_{Q_1} + e_{\bar{Q}_2} = e_\mathcal{M}$, where $e_\mathcal{M}$ is the charge of the scalar target and $e_{\bar{Q}_j} = -e_{Q_j}$.

While one may perform the manifestly covariant calculations of Eq. (15) using the Feynman parametrization, it has technical difficulties in analyzing the pole structures associated with the multidimensional integral of Feynman parameters. On the other hand, the LF calculations in $(1 + 1)$ dimensions avoid such difficulties since it involves only the one-dimensional integral, as we shall show below.

In terms of the LF variables, the s-channel amplitude $\mathcal{M}_s^\mu$ in Eq. (15) can be rewritten as

$$\mathcal{M}_s^\mu = \frac{ie_{Q_1}\mathcal{N}}{2(2\pi)^2} \int \frac{dk^+ dk^-}{C_s}$$
$$\times \frac{2k^\mu + q^\mu}{(k^- - k_i^-)(k^- - k_f^-)(k^- - k_t^-)(k^- - k_b^-)}, \quad (16)$$

where $C_s = k^+(k^+ + q^+)(k^+ - \Delta^+)(k^+ - p^+)$ and

$$k_i^- = \frac{m_{Q_1}^2}{k^+} - i\frac{\epsilon}{k^+},$$

$$k_f^- = \Delta^- + \frac{m_{Q_1}^2}{k^+ - \Delta^+} - i\frac{\epsilon}{k^+ - \Delta^+},$$

$$k_t^- = -q^- + \frac{m_{Q_1}^2}{k^+ + q^+} - i\frac{\epsilon}{k^+ + q^+},$$

$$k_b^- = p^- + \frac{m_{Q_2}^2}{k^+ - p^+} - i\frac{\epsilon}{k^+ - p^+}. \quad (17)$$

Similar expressions can be obtained for $\mathcal{M}_u^\mu$ and $\mathcal{M}_c^\mu$. The obtained 12 LF time-ordered diagrams for the scattering amplitudes $(\mathcal{M}_s^\mu, \mathcal{M}_u^\mu, \mathcal{M}_c^\mu)$ corresponding to (s, u, c)-channels are depicted in Fig. 2.

For the s-channel amplitude $\mathcal{M}_s^\mu$ in Eq. (16), the Cauchy integration over k^- gives the three LF time (x^+)-ordered contributions to the residue calculations, i.e., those coming from regions $S1$ $(\Delta^+ < k^+ < p^+)$, $S2$ $(-q^+ < k^+ < \Delta^+)$, and $S3$ $(0 < k^+ < -q^+)$, respectively. There are several comments in order. We note that q^+ in Eq. (6) is chosen to be $q^+ < 0$ and the region $S2$ is absent for the $\mu_s = 0$ limit as in the case of DVCS. The kinematic region $S1$ corresponds to the so-called DGLAP region [32–34], and the other two regions, $S2$ and $S3$, correspond to the so-called ERBL region [35–37]. The DGLAP and ERBL regions correspond to the valence contribution representing the particle-number-conserving process and the nonvalence one representing the particle-number-changing process, respectively.

In the DGLAP region of $S1$, where $\Delta^+ < k^+ < p^+$, the residue is at the pole of $k^- = k_b^-$, which is placed in the upper half of the complex k^- plane. Therefore, the Cauchy integration of $\mathcal{M}_s^\mu$ in Eq. (16) over k^- in this region leads to

$$\mathcal{M}_{s,\text{hand}}^\mu = -\frac{e_{Q_1}\mathcal{N}}{4\pi} \int_{\Delta^+}^{p^+} dk^+ \frac{2k_b^\mu + q^\mu}{C_s(\Delta k_{bi}^-)(\Delta k_{bf}^-)(\Delta k_{bt}^-)},$$
$$(18)$$

where $k_j^\mu = (k^+, k_j^-)$ and $\Delta k_{jk}^- = k_j^- - k_k^-$. This amplitude corresponds to the "handbag" diagram shown in Fig. 2(d) in the s-channel.

In the ERBL region of $S2$, where $-q^+ < k^+ < \Delta^+$, while two poles (k_i^-, k_t^-) are placed in the lower half of the complex k^- plane, the other two poles (k_f^-, k_b^-) lie on the upper half of the complex k^- plane. Taking the two poles $k^- = (k_f^-, k_b^-)$ and using some mathematical manipulations for the denominators, e.g., $1/(\Delta k_{fi}^- \Delta k_{fb}^-) = -(1/\Delta k_{bi}^-) \times (1/\Delta k_{fi}^- + 1/\Delta k_{bf}^-)$, we obtain two different types of LF time-ordered amplitudes in the $S2$ region as

$$\mathcal{M}_{s,\mathrm{stret}}^\mu = \frac{e_{Q_1}\mathcal{N}}{4\pi} \int_{-q^+}^{\Delta^+} dk^+ \frac{2k_i^\mu + q^\mu}{C_s(\Delta k_{bi}^-)(\Delta k_{fi}^-)(\Delta k_{ft}^-)},$$

$$\mathcal{M}_{s,\mathrm{open}}^\mu = \frac{e_{Q_1}\mathcal{N}}{4\pi} \int_{-q^+}^{\Delta^+} dk^+ \frac{2k_b^\mu + q^\mu}{C_s(\Delta k_{bi}^-)(\Delta k_{bt}^-)(\Delta k_{ft}^-)}, \quad (19)$$

where $\mathcal{M}_{s,\mathrm{stret}}^\mu$ and $\mathcal{M}_{s,\mathrm{open}}^\mu$ correspond to the so-called "stretched box" and "open diamond" diagrams shown in Figs. 2(b) and 2(c) in the s-channel, respectively.

In the other ERBL region of $S3$, where $0 < k^+ < -q^+$, the residue is at the pole of $k^- = k_i^-$, which is placed in the lower half of the complex k^- plane. The Cauchy integration of $\mathcal{M}_s^\mu$ in Eq. (16) over k^- in the $S3$ region leads to

$$\mathcal{M}_{s,\mathrm{twist}}^\mu = \frac{e_{Q_1}\mathcal{N}}{4\pi} \int_0^{-q^+} dk^+ \frac{2k_i^\mu + q^\mu}{C_s(\Delta k_{ib}^-)(\Delta k_{if}^-)(\Delta k_{it}^-)}, \quad (20)$$

which corresponds to what we call the "twisted stretched box" diagram as shown in Fig. 2(a) in the s-channel.

Similarly, we can obtain the LF time-ordered amplitudes for $\mathcal{M}_u^\mu$ of Figs. 2(e)–2(h) in the u-channel and $\mathcal{M}_c^\mu$ of Figs. 2(i)–2(l) in the c-channel. Their explicit expressions read

$$\mathcal{M}_{u,\mathrm{twist}}^\mu = \frac{e_{Q_1}\mathcal{N}}{4\pi} \int_0^{q'^+} dk^+ \frac{2k_i^\mu - 2q'^\mu + q^\mu}{C_u(\Delta k_{if}^-)(\Delta k_{iu}^-)(\Delta k_{ib}^-)},$$

$$\mathcal{M}_{u,\mathrm{stret}}^\mu = -\frac{e_{Q_1}\mathcal{N}}{4\pi} \int_{q'^+}^{\Delta^+} dk^+ \frac{2k_i^\mu - 2q'^\mu + q^\mu}{C_u(\Delta k_{ib}^-)(\Delta k_{fi}^-)(\Delta k_{fu}^-)},$$

$$\mathcal{M}_{u,\mathrm{open}}^\mu = -\frac{e_{Q_1}\mathcal{N}}{4\pi} \int_{q'^+}^{\Delta^+} dk^+ \frac{-2k_b^\mu + 2q'^\mu - q^\mu}{C_u(\Delta k_{ub}^-)(\Delta k_{fu}^-)(\Delta k_{ib}^-)},$$

$$\mathcal{M}_{u,\mathrm{hand}}^\mu = -\frac{e_{Q_1}\mathcal{N}}{4\pi} \int_{\Delta^+}^{p^+} dk^+ \frac{2k_b^\mu - 2q'^\mu + q^\mu}{C_u(\Delta k_{bf}^-)(\Delta k_{bu}^-)(\Delta k_{bi}^-)},$$

$$(21)$$

and

$$\mathcal{M}_{c(i)}^\mu = -\frac{e_{\bar{Q}_2}\mathcal{N}}{4\pi} \int_0^{q'^+} dk^+ \frac{2k_i^\mu - 2p^\mu - q^\mu}{C_c(\Delta k_{ib}^-)(\Delta k_{ic}^-)(\Delta k_{iu}^-)},$$

$$\mathcal{M}_{c(j)}^\mu = \frac{e_{\bar{Q}_2}\mathcal{N}}{4\pi} \int_{q'^+}^{p^++q^+} dk^+ \frac{-2k_i^\mu + 2p^\mu + q^\mu}{C_c(\Delta k_{bi}^-)(\Delta k_{ci}^-)(\Delta k_{cu}^-)},$$

$$\mathcal{M}_{c(k)}^\mu = \frac{e_{\bar{Q}_2}\mathcal{N}}{4\pi} \int_{q'^+}^{p^++q^+} dk^+ \frac{-2k_b^\mu + 2p^\mu + q^\mu}{C_c(\Delta k_{bi}^-)(\Delta k_{bu}^-)(\Delta k_{cu}^-)},$$

$$\mathcal{M}_{c(l)}^\mu = \frac{e_{\bar{Q}_2}\mathcal{N}}{4\pi} \int_{p^++q^+}^{p^+} dk^+ \frac{2k_b^\mu - 2p^\mu - q^\mu}{C_c(\Delta k_{bc}^-)(\Delta k_{bu}^-)(\Delta k_{bi}^-)}, \quad (22)$$

where $C_u = k^+(k^+ - q'^+)(k^+ - \Delta^+)(k^+ - p^+)$, $C_c = k^+(k^+ - q'^+)(k^+ - p^+ - q^+)(k^+ - p^+)$, and

$$k_u^- = q'^- + \frac{m_{Q_1}^2}{k^+ - q'^+} - i\frac{\epsilon}{k^+ - q'^+},$$

$$k_c^- = p^- + q^- + \frac{m_{Q_2}^2}{k^+ - p^+ - q^+} - i\frac{\epsilon}{k^+ - p^+ - q^+}. \quad (23)$$

B. Amplitudes from effective tree diagrams

For the neural target, where $e_\mathcal{M} = e_{Q_1} + e_{\bar{Q}_2} = 0$, the gauge invariance condition $q \cdot \mathcal{M}_{\mathrm{tot}}^\mu = 0$ is guaranteed when $\mathcal{M}_{\mathrm{tot}}^\mu = \mathcal{M}_{\mathrm{loop}}^\mu$. However, for the case of a charged target such as the "helium" nucleus, additional diagrams called "effective tree" diagrams, where the photon line is attached to the charged target, are required to ensure the gauge invariance. The effective tree contribution to the scattering amplitude is decomposed as

$$\mathcal{M}_{\mathrm{ET}}^\mu = \mathcal{M}_{s,\mathrm{ET}}^\mu + \mathcal{M}_{u,\mathrm{ET}}^\mu, \quad (24)$$

where the corresponding LF time-ordered diagrams are presented in Fig. 3. The covariant scattering amplitudes $\mathcal{M}_{s,\mathrm{ET}}^\mu$ and $\mathcal{M}_{u,\mathrm{ET}}^\mu$ are obtained as

$$\mathcal{M}_{s,\mathrm{ET}}^\mu = \frac{ie_\mathcal{M}\mathcal{N}}{(p+q)^2 - M_T^2} \int \frac{d^2k}{(2\pi)^2} \frac{2p^\mu + q^\mu}{N_k N_{k-q'} D_{k-p-q}},$$

$$\mathcal{M}_{u,\mathrm{ET}}^\mu = \frac{ie_\mathcal{M}\mathcal{N}}{(p-q')^2 - M_T^2} \int \frac{d^2k}{(2\pi)^2} \frac{2p^\mu + q^\mu - 2q'^\mu}{N_k N_{k-q'} D_{k-p}}. \quad (25)$$

In the LF calculations, the Cauchy integration over k^- in Eq. (25) gives two LF time-ordered contributions to the residue calculations. For $\mathcal{M}_{s,\mathrm{ET}}^\mu$, one comes from the valence region $(q'^+ < k^+ < p^+ + q^+)$ as shown in Fig. 3(a) and the other from the nonvalence region $(0 < k^+ < q'^+)$ as shown in Fig. 3(b). In the case of $\mathcal{M}_{u,\mathrm{ET}}^\mu$, they come from the valence region $(q'^+ < k^+ < p^+)$ as shown in Fig. 3(c) and from the nonvalence region $(0 < k^+ < q'^+)$ as shown in Fig. 3(d). In the valence (nonvalence) region for $\mathcal{M}_{s,\mathrm{ET}}^\mu$, the residue is at the pole of $k^- = k_c^-(k_i^-)$, which
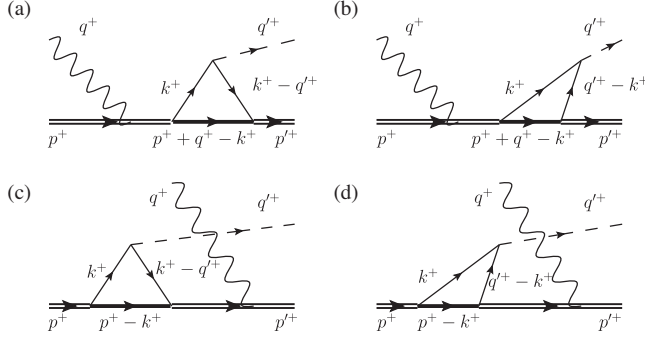
FIG. 3. The LF time-ordered effective tree diagrams in the s- and u-channels for a charged target case. (a),(b) The valence and nonvalence contributions to $\mathcal{M}^\mu_{s,\text{ET}}$, respectively, and (c),(d) the valence and nonvalence contributions to $\mathcal{M}^\mu_{u,\text{ET}}$, respectively.

is placed in the upper (lower) half of the complex k^- plane. Similarly, in the valence (nonvalence) region for $\mathcal{M}^\mu_{u,\text{ET}}$, the residue is at the pole of $k^- = k_b^-(k_i^-)$, which is placed in the upper (lower) half of the complex k^- plane. Thus, the Cauchy integrations of $\mathcal{M}^\mu_{s(u),\text{ET}}$ over k^- lead to

$$\mathcal{M}^\mu_{s,\text{ET}} = \frac{e_\mathcal{M}\mathcal{N}}{4\pi[(p+q)^2 - M_T^2]}\left[\int_0^{q'^+} dk^+ \frac{2p^\mu + q^\mu}{C_s'(\Delta k_{iu}^-)(\Delta k_{ic}^-)}\right.$$
$$\left. - \int_{q'^+}^{p^+ + q^+} dk^+ \frac{2p^\mu + q^\mu}{C_s'(\Delta k_{ci}^-)(\Delta k_{cu}^-)}\right],$$

$$\mathcal{M}^\mu_{u,\text{ET}} = \frac{e_\mathcal{M}}{4\pi[(p-q')^2 - M_T^2]}\left[\int_0^{q'^+} dk^+ \frac{2p^\mu + q^\mu - 2q'^\mu}{C_u'(\Delta k_{iu}^-)(\Delta k_{ib}^-)}\right.$$
$$\left. - \int_{q'^+}^{p^+} dk^+ \frac{2p^\mu + q^\mu - 2q'^\mu}{C_u'(\Delta k_{bi}^-)(\Delta k_{bu}^-)}\right], \quad (26)$$

where $C_s' = k^+(k^+ - q'^+)(k^+ - p^+ - q^+)$ and $C_u' = k^+(k^+ - q'^+)(k^+ - p^+)$.

It should be noted that the full amplitudes are obtained by including the exchanged diagrams $(Q_1 \leftrightarrow Q_2)$ in Figs. 1–3. Although we do not give the corresponding amplitudes explicitly, their expressions can straightforwardly be obtained from the formulas given above with the exchange of $Q_1 \leftrightarrow Q_2$. It should be understood that the contributions from the exchange of $Q_1 \leftrightarrow Q_2$ are included in our numerical computation of the full amplitudes even if they are not explicitly mentioned. Thus, the total scattering amplitudes for the neutral and charged targets may be summarized as

$$\mathcal{M}^\mu_{\text{neutral}} = \mathcal{M}^\mu_{\text{loop}}(Q_1, Q_2) + (1 \leftrightarrow 2),$$
$$\mathcal{M}^\mu_{\text{charged}} = \mathcal{M}^\mu_{\text{loop}}(Q_1, Q_2) + \mathcal{M}^\mu_{\text{ET}}(Q_1, Q_2) + (1 \leftrightarrow 2),$$
$$(27)$$

respectively. The CFF $\mathcal{F}_c$ for the charged target such as the helium nucleus is then computed by

$$\mathcal{F}^{\text{VMP}}_c(Q^2, t) = \frac{\mathcal{M}^\mu_{\text{charged}}}{(\Delta \cdot q)q^\mu - q^2\Delta^\mu}, \quad (28)$$

which is valid for each component ($\mu = +, -$) of the current in (1 + 1) dimensions.

IV. DEEPLY VIRTUAL MESON PRODUCTION LIMIT

In this section, we analyze the amplitude in the DVMP limit, where Q^2 is larger than the other scales, namely, $Q^2 \gg (M_T^2, M_S^2, -t)$. From $Q^2 \gg (M_S^2, -t)$, we have $(\mu_s, \tau) \to 0$, which leads to $\zeta = \zeta'$, $q^- = q'^- = Q^2/\zeta p^+$, $q^+ = -\Delta^+$, and $q'^+ = 0$ from Eqs. (6) and (7). Furthermore, we also have $\Delta k_{bt}^- = \Delta k_{ft}^- = \Delta k_{it}^- = q^-$ in the energy denominators for the scattering amplitudes given by Eqs. (18)–(20). However, it should be noted that the condition $Q^2 \gg M_T^2$ is not used here in taking the DVMP limit.

A. Generalized parton distribution

In the DVMP limit, the time-ordered amplitudes for the s-channel with $\mu = +$ given by Eqs. (18)–(20) are now reduced to

$$\mathcal{M}^{+\text{DVMP}}_{s,\text{hand}} = \frac{e_{Q_1}\mathcal{N}}{4\pi q^-} \int_{\Delta^+}^{p^+} dk^+ \frac{-2k^+ + \Delta^+}{C_s(k_b^- - k_i^-)(k_b^- - k_f^-)},$$

$$\mathcal{M}^{+\text{DVMP}}_{s,\text{twist}} = \frac{e_{Q_1}\mathcal{N}}{4\pi q^-} \int_0^{\Delta^+} dk^+ \frac{2k^+ - \Delta^+}{C_s(k_i^- - k_b^-)(k_i^- - k_f^-)}, \quad (29)$$

at the leading order in Q^2, where we have used $q^+ = -\Delta^+$. The kinematic region for both the open diamond and stretched box diagrams given by Eq. (19) vanishes in the limit of $q^+ = -\Delta^+$. Also, the effective tree amplitude $\mathcal{M}^{+\text{DVMP}}_{s,\text{ET}}$ in Eq. (26) does not contribute in the DVMP limit.

Similarly, the reduced amplitudes for the u-channel in the DVMP limit are given by

$$\mathcal{M}^{+\text{DVMP}}_{u,\text{hand}} = \frac{e_{Q_1}\mathcal{N}}{4\pi q^-} \int_{\Delta^+}^{p^+} dk^+ \frac{2k^+ - \Delta^+}{C_u(k_b^- - k_i^-)(k_b^- - k_f^-)},$$

$$\mathcal{M}^{+\text{DVMP}}_{u,\text{stret}} = \frac{e_{Q_1}\mathcal{N}}{4\pi q^-} \int_0^{\Delta^+} dk^+ \frac{-2k^+ + \Delta^+}{C_u(k_i^- - k_b^-)(k_i^- - k_f^-)} \quad (30)$$

from Eq. (21). Neither the effective tree amplitude $\mathcal{M}^{+\text{DVMP}}_{u,\text{ET}}$ in Eq. (26) nor the amplitudes of the cat's ears in Eq. (22) contribute in the DVMP limit.

Combining both s- and u-channel amplitudes given by Eqs. (29) and (30) and using the longitudinal momentum fraction $x = k^+/p^+$ ($0 \le x \le 1$), we obtain the DVMP amplitude in the leading order of Q^2 as the factorized form of the hard and soft parts given by

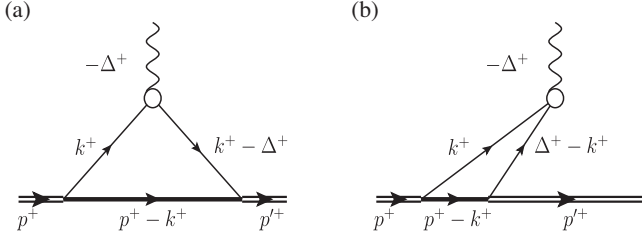(a)   (b)

FIG. 4. Diagrams for GPDs in different kinematic regions for the $\zeta > 0$ case. The sum of $\mathcal{M}_{s,\text{hand}}^{+\text{DVMP}}$ and $\mathcal{M}_{u,\text{hand}}^{+\text{DVMP}}$ corresponds to the valence diagram (a) defined in the DGLAP ($\zeta \leq x \leq 1$) region and the sum of $\mathcal{M}_{s,\text{twist}}^{+\text{DVMP}}$ and $\mathcal{M}_{u,\text{stret}}^{+\text{DVMP}}$ corresponds to the nonvalence diagram (b) defined in the ERBL ($0 \leq x \leq \zeta$) region. The small white blob in the figure represents the nonlocality of the constituent–gauge-boson vertex.

$$\mathcal{M}_{s+u}^{+\text{DVMP}} = \frac{e_{Q_1}\zeta}{4\pi Q^2} \int_0^1 dx \left(\frac{1}{x-\zeta} - \frac{1}{x} \right) H(\zeta, x, t), \quad (31)$$

where

$$H(\zeta, x, t) = \begin{cases} H_{\text{ERBL}}(\zeta, x, t), & \text{for } 0 \leq x \leq \zeta, \\ H_{\text{DGLAP}}(\zeta, x, t), & \text{for } \zeta \leq x \leq 1 \end{cases} \quad (32)$$

is identified as the GPD [4–11]. The GPD function $H(\zeta, x, t)$ is naturally represented by the sum of the LF nonvalence contribution to the ERBL ($0 \leq x \leq \zeta$) region and the valence contribution to the DGLAP ($\zeta \leq x \leq 1$) region as shown in Fig. 4.

Respectively, $H_{\text{ERBL}}(\zeta, x, t)$ and $H_{\text{DGLAP}}(\zeta, x, t)$ are given by

$$H_{\text{ERBL}} = \frac{\mathcal{N}}{x(\zeta - x)(1-x)} \frac{(2x - \zeta)\zeta}{(M_T^2 - M_0^2)\left(t + \frac{\zeta^2 m_{Q_1}^2}{x(x-\zeta)}\right)},$$

$$H_{\text{DGLAP}} = \frac{\mathcal{N}}{x(x - \zeta)(1-x)} \frac{(2x - \zeta)(1-\zeta)}{(M_T^2 - M_0^2)(M_T^2 - M_0'^2)}, \quad (33)$$

where

$$M_0^2 = \frac{m_{Q_1}^2}{x} + \frac{m_{Q_2}^2}{1-x}, \qquad M_0'^2 = \frac{m_{Q_1}^2}{x'} + \frac{m_{Q_2}^2}{1-x'} \quad (34)$$

with $x' = (x - \zeta)/(1 - \zeta)$. It can be checked that $H_{\text{ERBL}}(\zeta, x, t)$ and $H_{\text{DGLAP}}(\zeta, x, t)$ obtained in this model are continuous and finite at the boundary $x = \zeta$, namely, $H_{\text{ERBL}}(\zeta, \zeta, t) = H_{\text{DGLAP}}(\zeta, \zeta, t) = H(\zeta, \zeta, t)$, which is written explicitly as

$$H(\zeta, \zeta, t) = \frac{\mathcal{N}\zeta}{(1-\zeta)m_{Q_1}^4 + \zeta m_{Q_1}^2[m_{Q_2}^2 + (\zeta - 1)M_T^2]}. \quad (35)$$

It is related with the imaginary part of the DVMP amplitude $\mathcal{M}_{s+u}^{+\text{DVMP}}$ in Eq. (31). As we have mentioned in Sec. II,

ζ and t are not independent of each other in $(1+1)$ dimensions unlike the $(3+1)$-dimensional case and the explicit expression in Eq. (35) is given by a function of ζ only.

In the DVMP limit and at the leading order of Q^2, the contributions from effective tree amplitudes are suppressed and only the s- and u-channel loop amplitudes contribute. Effectively, the DVMP results given by $\mathcal{M}_{s+u}^{+\text{DVMP}}$ are independent of the electric charge of the target, whether it is charged or neutral. Taking into account the corresponding prefactor in Eq. (13) relating the scattering amplitude to the CFF given by

$$(\Delta \cdot q)q^+ - q^2\Delta^+ = \frac{1}{2}Q^2\zeta p^+ \left[1 + \frac{t}{Q^2} + \cdots\right], \quad (36)$$

we obtain the CFF in the DVMP limit at the leading order of Q^2 denoted by $\mathcal{F}^{\text{DVMP}}$ as

$$\mathcal{F}^{\text{DVMP}}(Q^2, t) = \frac{\mathcal{M}_{s+u}^{+\text{DVMP}}}{\frac{1}{2}Q^2\zeta p^+}. \quad (37)$$

In view of the QCD collinear factorization theorem at the leading twist for the DVMP process [38], the comparison of $\mathcal{F}^{\text{DVMP}}(Q^2, t)$ of Eq. (37) with the exact results $\mathcal{F}_c(Q^2, t)$ of Eq. (28) would be very interesting as it allows us to explore the valid kinematic region for the GPD formulation based on the handbag dominance in the leading order of Q^2. We compare the numerical results of $\mathcal{F}_c$ and the leading twist $\mathcal{F}^{\text{DVMP}}(Q^2, t)$ in Sec. V.

B. Parton distribution functions

In the limit $(\zeta, t) \to 0$, we have $H(0, x, 0) = H_{\text{DGLAP}}(0, x, 0) \equiv q_v(x)$, where

$$q_v(x) = \frac{2\mathcal{N}}{x(1-x)(M_T^2 - M_0^2)^2}. \quad (38)$$

In this limit, $H_{\text{ERBL}}(0, x, 0) = 0$ and $q_v(x)$ corresponds to the ordinary PDF representing the probability to find the constituent inside the hadron as a function of the momentum fraction x carried by the constituent in the valence sector. The corresponding LF wave function $\psi(x)$ of the target hadron in the momentum space may be written as

$$\psi(x) = \sqrt{q_v(x)}, \quad (39)$$

which satisfies $\int_0^1 dx |\psi(x)|^2 = \frac{1}{2}\int_{-1}^1 dy q_v(y) = 1$. We then obtain the nth moment of $q_v(x)$ defined by [39]

$$\langle y_n \rangle = \int_{-1}^1 dy \, y^n q_v(y), \quad (40)$$

where $y = 2x - 1$.

Introducing the longitudinally boost-invariant dimensionless LF spatial variable $\tilde{z} = p^+ x^-$, which is canonically conjugate to x [31,40,41], the LF wave function $\psi(\tilde{z})$ in the LF coordinate space $\tilde{z}$ evaluated at $x^+ = 0$ can be defined by

$$\psi(\tilde{z}) = \frac{1}{\sqrt{2\pi}} \int dx\, \psi(x) e^{ik \cdot x} = \frac{1}{\sqrt{2\pi}} \int_0^1 dx\, \psi(x) e^{i\tilde{z}x/2} \tag{41}$$

as the Fourier transform of $\psi(x)$ in (1 + 1) dimensions. Then, the longitudinal probability density $\varrho(\tilde{z})$ in the LF coordinate space $\tilde{z}$ is given by

$$\varrho(\tilde{z}) = |\psi(\tilde{z})|^2, \tag{42}$$

which satisfies $\int_0^\infty \varrho(\tilde{z}) d\tilde{z} = 1$. Detailed discussions on the three-dimensional version of Eq. (41), $\varrho(\tilde{z}, \mathbf{b})$, which includes the transverse distance $\mathbf{b}$ of the struck constituent from the transverse center of momentum, were provided in Refs. [31,40,41].

C. Moments of GPD

In general, the nth moment of the GPD is defined by

$$F_n(\zeta, t) = \int_0^1 \frac{dx}{1 - \zeta/2} x^{n-1} H(\zeta, x, t). \tag{43}$$

It is well known that the polynomiality conditions [42,43] for the nth moment of the GPD require that the highest power of ζ in the polynomial expression of $F_n(\zeta, t)$ should not be larger than n. These polynomiality conditions are fundamental properties of the GPD, which follow from the Lorentz invariance.

The first moment of $H(\zeta, x, t)$ is related to the EM form factor $F_{\mathcal{M}}(t)$ of the target $\mathcal{M}$ by the following sum rule [4–7]:

$$F_{\mathcal{M}}(t) = \int_0^1 \frac{dx}{1 - \zeta/2} H(\zeta, x, t). \tag{44}$$

In the (3 + 1)-dimensional analysis, the full result of the EM form factor ($n = 1$) should be independent of ζ so that $F_1(\zeta, t) = F_{\mathcal{M}}(t)$ since the two variables ζ and t are independent of each other. However, in (1 + 1) dimensions, the moment $F_n(\zeta, t)$ should be a function of a single variable, $F_n(\zeta)$ or $F_n(t)$, since the two variables are related to each other. For example, $\zeta = 0$ and 1 correspond to $-t = 0$ and ∞, respectively. In other words, the interval of $\zeta = [0, 1]$ covers the entire range of the momentum transfer squared $-t = [0, \infty]$ in the nth moment of the GPD in (1 + 1) dimensions. Furthermore, all the moments vanish at $\zeta = 1$, i.e., $F_n(\zeta = 1) = 0$, which hinders checking the polynomiality conditions. To circumvent this hindrance in checking the polynomiality conditions due to $F_n(\zeta = 1) = 0$, we redefine the moments as

$$\bar{F}_n(\zeta) = F_n(\zeta)/F_1(\zeta), \tag{45}$$

so that $\bar{F}_1(\zeta)$ is independent of ζ. In Sec. V, we will discuss how our model calculations for $\bar{F}_n(\zeta)$ satisfy the polynomiality conditions.

The normalization factor $\mathcal{N}$ is fixed by the condition $F_{\mathcal{M}}(0) = 1$ and given by

$$\mathcal{N} = \frac{m_{Q_1}^2 m_{Q_2}^2 (1 - \omega^2)^2}{1 - \omega^2 + \omega\sqrt{1 - \omega^2} T_\omega}, \tag{46}$$

where

$$\omega = \frac{M_T^2 - m_{Q_2}^2 - m_{Q_1}^2}{2 m_{Q_1} m_{Q_2}}, \tag{47}$$

and

$$T_\omega = \tan^{-1}\left(\frac{m_{Q_2} + m_{Q_1}\omega}{m_{Q_1}\sqrt{1 - \omega^2}}\right) + \tan^{-1}\left(\frac{m_{Q_1} + m_{Q_2}\omega}{m_{Q_2}\sqrt{1 - \omega^2}}\right). \tag{48}$$

We note that the EM form factor obtained by using Eqs. (32)–(33) and Eq. (44) is identical to the form factor obtained in our previous publication [23] within the same solvable ϕ^3 scalar field model in (1 + 1) dimensions [24,25,27].

V. NUMERICAL RESULTS

For the numerical computation, we simulate the electroproduction of a scalar meson $f_0(980)$ off the scalar target ^{4}He with the electric charge $e_{\mathcal{M}} = +2e$ using the (1 + 1)-dimensional scalar field theory discussed in the present work. For our numerical calculations and analyses, we thus take the target and scalar meson masses as $M_T = 3.7$ GeV and $M_S = 0.98$ GeV. In this case, the threshold momentum transfer at $Q^2 = 0$ is given by $t_{\text{th}}(Q^2 = 0) = -M_T M_S^2/(M_T + M_S) \simeq -0.76$ GeV^2. For the constituent mass, we use the equal mass for both constituents, $m_{Q_1} = m_{Q_2} = 2$ GeV, so that the ^{4}He target is a weakly bound state, as $M_T < m_{Q_1} + m_{Q_2}$ but $M_T^2 > m_{Q_1}^2 + m_{Q_2}^2$.[3] However, we will discuss the cases with some variations of constituent masses as needed for comments. For the consistency of our numerical analysis, we use the same normalization constant $\mathcal{N}$ given by Eq. (46) for all physical observables such as the CFF $\mathcal{F}(Q^2, t)$, the GPD $H(\zeta, x, t)$, and the EM form factor $F_{\mathcal{M}}(t)$ throughout the present work.

---

[3]Therefore, we mimic the reaction of $f_0(980)$ production off the ^{4}He targets in (1 + 1) dimensions assuming that the ^{4}He nucleus is a bound state of two (scalar) deuterons.
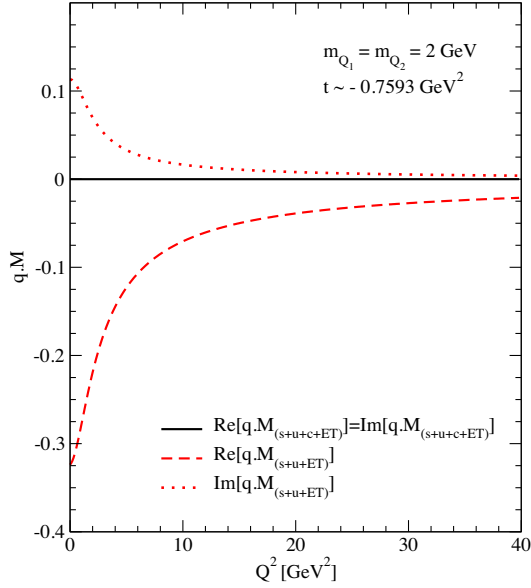
FIG. 5. Role of the c-channel contributions in the gauge invariance condition of $\mathrm{Re}[q \cdot \mathcal{M}]$ and $\mathrm{Im}[q \cdot \mathcal{M}]$ for a charged target. The solid line is for the full amplitude while the dashed and dotted lines are for the amplitudes without the c-channel contributions.

A. CFF in VMP

As we have discussed before, the total scattering amplitude for a charged target $\mathcal{M}^\mu = \mathcal{M}^\mu_{\mathrm{charged}}$ given by Eq. (27), i.e., the full results without any approximation, should satisfy the gauge invariance condition $q \cdot \mathcal{M} = 0$. Furthermore, since $\mathcal{M}^\mu$ is in general a complex-valued function, even for the spacelike region $Q^2 > 0$, the real and imaginary part of $\mathcal{M}^\mu$ can be shown to satisfy the gauge invariance condition separately, i.e., $\mathrm{Re}[q \cdot \mathcal{M}] = 0$ and $\mathrm{Im}[q \cdot \mathcal{M}] = 0$. We first check numerically whether these conditions are met by our amplitudes. The solid line of Fig. 5 shows that the gauge invariance is observed by the exact amplitude $\mathcal{M}^\mu_{\mathrm{charged}} = \mathcal{M}^\mu_{u+s+c+\mathrm{ET}}$ for the range of $0 \le Q^2 \le 40$ GeV^2 at $t = t_{\mathrm{th}}(Q^2 = 0)$. To estimate the c-channel contribution, we turn off the c-channel contributions, and the results for the real and imaginary parts of $q \cdot \mathcal{M}_{u+s+\mathrm{ET}}$ are plotted by the dashed and dotted lines, respectively, in Fig. 5. This evidently shows that the omission of the cat's ears diagrams violates the Ward identity. The violation is more serious at the smaller Q^2 region, although the degree of deviation weakens at the larger Q^2 region as anticipated.

We then compute the CFF in VMP, $\mathcal{F}^{\mathrm{VMP}}_c(Q^2, t)$. Shown in Fig. 6 are the real part, the imaginary part, and the modulus of the amplitude $\mathcal{F}^{\mathrm{VMP}}_c$ obtained from $\mathcal{M}^+_{\mathrm{charged}}$ of Eq. (28) in the range of $0 \le Q^2 \le 10$ GeV^2 at $t = t_{\mathrm{th}}(Q^2 = 0) \simeq -0.7593$ GeV^2. In order to explore the sensitivity of $\mathcal{F}^{\mathrm{VMP}}_c(Q^2, t)$ on the constituent mass, we vary the constituent mass and repeat the computations for $m_{Q_1} = 1.9$, 2.0, and

2.1 GeV, while keeping $m_{Q_1} = m_{Q_2}$.[4] The results for $m_{Q_1} = 1.9$, 2.0, and 2.1 GeV are presented by the dot-dashed, solid, and dashed lines, respectively. The close inspection of Fig. 6 leads to the following comments. (i) The real part has a hump structure, and the peak locates at the higher values of Q^2 with the lesser pronounced hump structures as the binding energy increases, as shown in Fig. 6(a). (ii) The magnitude of the imaginary part gets larger as the binding energy increases as shown in Fig. 6(b). (iii) As a result, the hump behavior of $|\mathcal{F}^{\mathrm{VMP}}_c(Q^2, t)|$ shown in Fig. 6(c) appears strong near $Q^2 \simeq |t_{\mathrm{th}}(Q^2 = 0)|$ for weak binding energies, but it goes away as the binding energy increases. Also, there is no hump structure in the $|\mathcal{F}^{\mathrm{VMP}}_c(Q^2, t)|$ for $Q^2 > |t_{\mathrm{th}}(Q^2 = 0)|$ region and the binding energy effect is getting smaller as Q^2 increases.

The left and right panels of Fig. 7, respectively, show the three-dimensional and contour plots of $\mathrm{Re}[\mathcal{F}^{\mathrm{VMP}}_c]$, $\mathrm{Im}[\mathcal{F}^{\mathrm{VMP}}_c]$, and $|\mathcal{F}^{\mathrm{VMP}}_c|$ for the range of $0 \le Q^2 \le 20$ GeV^2 and -2 GeV$^2 \le t \le 0$. Both the real (top panel) and imaginary (middle panel) parts are going to zero as $t \to 0$ regardless of the value of Q^2. For $|t| \lesssim Q^2$, the real part of $\mathcal{F}^{\mathrm{VMP}}_c$ shows a gradual crest along the straight line of $|t| \approx Q^2$, and the imaginary part has a trough located at $|t| \approx Q^2$. Both the real and imaginary parts rapidly approach zero as $|t|$ decreases to zero for the small Q^2 region from the crest and trough, respectively. The modulus of the CFF also has a crest around $|t| \approx Q^2$ and gradually decreases as Q^2 increases and $|t|$ decreases.

B. CFF and GPD in the DVMP limit

In the DVMP limit, where $Q^2 \gg (M^2_S, |t|)$ but not explicitly involving $Q^2 \gg M^2_T$ due to the correlation among ζ_{1+1}, t and M^2_T as discussed in Sec. II, the scattering amplitude for the scalar meson production from either the neutral or charged scalar target is reduced to the DVMP amplitude $\mathcal{M}^{+\mathrm{DVMP}}_{s+u}$. Regardless of neutral or charged target, the s- and u-channel amplitudes are factorized in the DVMP limit as discussed in Sec. IV A and $\mathcal{M}^{+\mathrm{DVMP}}_{s+u}$ is given by the factorized form of the hard scattering part and the soft GPD $H(\zeta, x, t)$ as shown in Eq. (31). In order to find the region where the DVMP limit is valid, we compare the CFF $\mathcal{F}^{\mathrm{DVMP}}$ in Eq. (37) obtained from $\mathcal{M}^{+\mathrm{DVMP}}_{s+u}$ with the exact solution $\mathcal{F}^{\mathrm{VMP}}_c$ presented in Fig. 6.

In Fig. 8, we compare $\mathcal{F}^{\mathrm{VMP}}_c$ (solid lines) and the leading twist $\mathcal{F}^{\mathrm{DVMP}}$ (dashed lines) for the range of $0 \le Q^2 \le 10$ GeV^2. Figures 8(a), 8(c) and 8(b), 8(d) show $(\mathrm{Re}[\mathcal{F}], \mathrm{Im}[\mathcal{F}])$, at $t = t_{\mathrm{th}}(Q^2 = 0) \simeq -0.7593$ GeV^2 and $t = -2$ GeV^2, respectively. There are several points to comment on the results shown in Fig. 8. (i) While the exact solution $\mathcal{F}^{\mathrm{VMP}}_c$ is finite at $Q^2 = 0$ with a hump

---

[4]These masses give the binding energy $B = m_{Q_1} + m_{Q_2} - M_T$ in the range of (0.1–0.5) GeV.
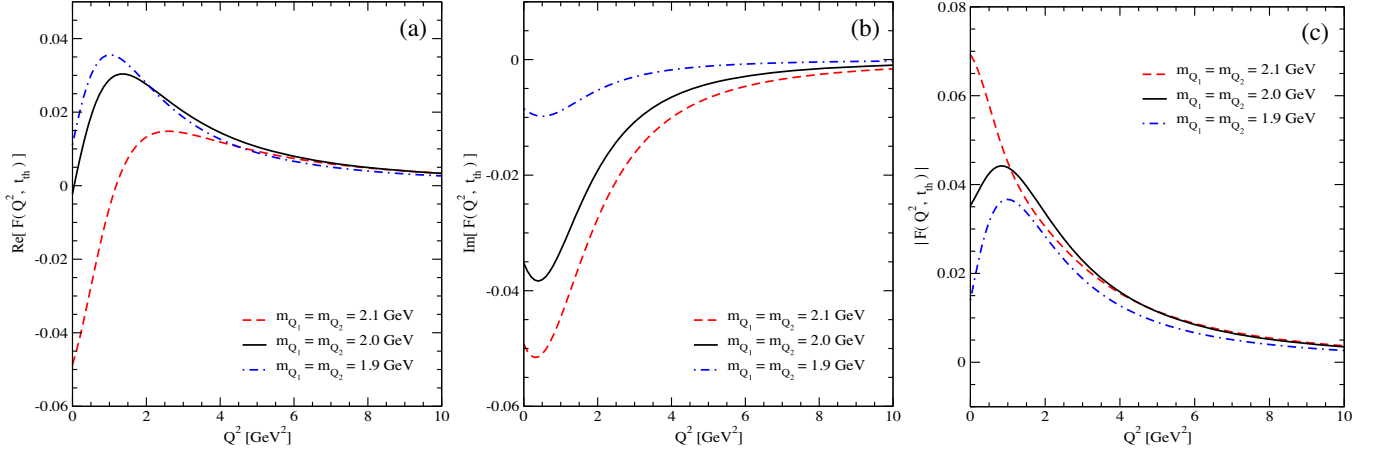
FIG. 6. The Compton form factor $\mathcal{F}_c^{\mathrm{VMP}}(Q^2, t)$. (a) Its real part, (b) its imaginary part, and (c) its modulus for three constituent masses, $m_{Q_1} = m_{Q_2} = 1.9$, 2.0, and 2.1 GeV at the momentum transfer squared $t = t_{\mathrm{th}} \simeq -0.7593$ GeV^2.

behavior near $Q^2 = -t$, the results of $\mathcal{F}^{\mathrm{DVMP}}$ obtained at the leading order of Q^2 in the DVMP limit do not have any hump structure but blow up in the vicinity of $Q^2 = 0$. (ii) The agreement between $\mathcal{F}_c^{\mathrm{VMP}}$ and $\mathcal{F}^{\mathrm{DVMP}}$ can be seen at the large Q^2 region, but it reaches faster as the smaller $-t$ value is used. For instance, the VMP and DVMP results agree for $Q^2 \geq 6$ GeV^2 when $-t \simeq 0.7593$ GeV^2 is fixed.

This indicates that the validity of the GPD handbag approximation is governed by $-t/Q^2$, but not separately by $-t$ or by Q^2. Figure 8 shows that it is valid in the region of $-t/Q^2 \leq 0.125$ with $-t \simeq 0.7593$ GeV^2. On the other hand, for $-t \simeq 2$ GeV^2, the agreement of the VMP and DVMP CFFs can be seen at higher Q^2, i.e., $Q^2 > 10$ GeV^2, which corresponds to $-t/Q^2 \simeq 0.2$. To have better agreement for both the real and imaginary parts of the CFF, Q^2
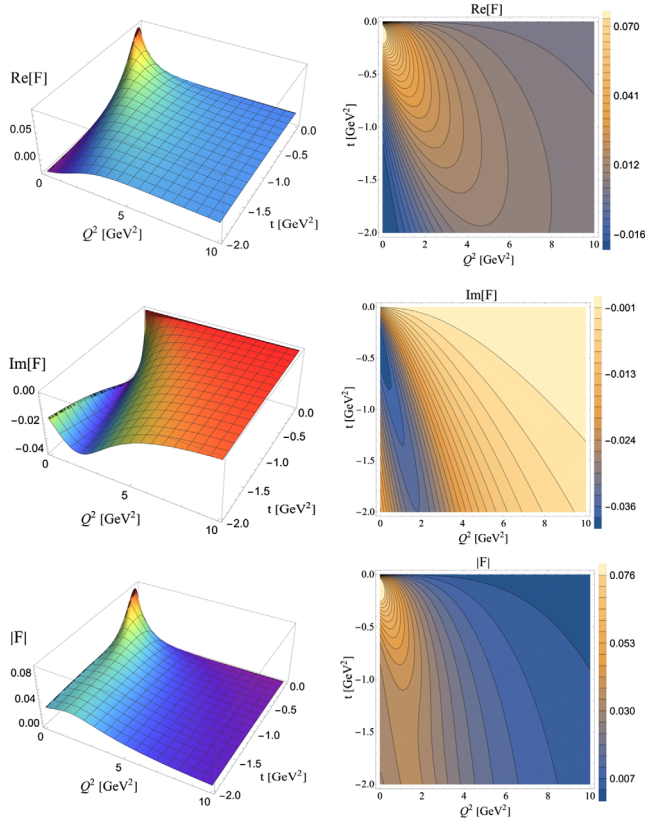

FIG. 7. (Left) Three-dimensional and (right) contour plots for the real part, imaginary part, and modulus of the Compton form factor $\mathcal{F}_c^{\mathrm{VMP}}$.
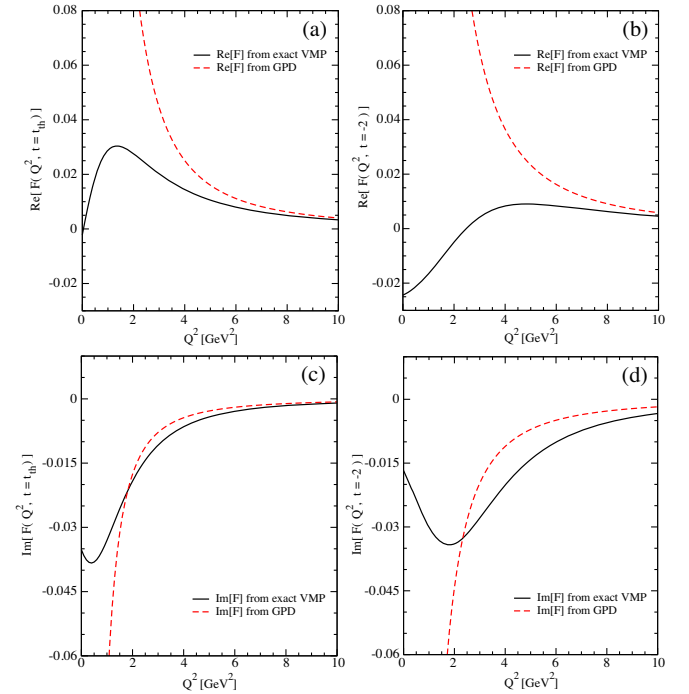

FIG. 8. The real and imaginary parts of the Compton form factor determined from $\mathcal{M}_{s+u+c+ET}^+$ and $\mathcal{M}^{+DVMP}$. (a) $\mathrm{Re}[\mathcal{F}(Q^2)]$ for $t = t_{\mathrm{th}} \simeq -0.7593$ GeV^2, (b) $\mathrm{Re}[\mathcal{F}(Q^2)]$ for $t = -2$ GeV^2, (c) $\mathrm{Im}[\mathcal{F}(Q^2)]$ for $t = t_{\mathrm{th}} \simeq -0.7593$ GeV^2, and (d) $\mathrm{Im}[\mathcal{F}(Q^2)]$ for $t = -2$ GeV^2.

FIG. 10. The ordinary valence PDF $q_v(x)$ of the scalar target multiplied by x for $m_{Q_1} = m_{Q_2} = 1.9$, 2.0, and 2.1 GeV.

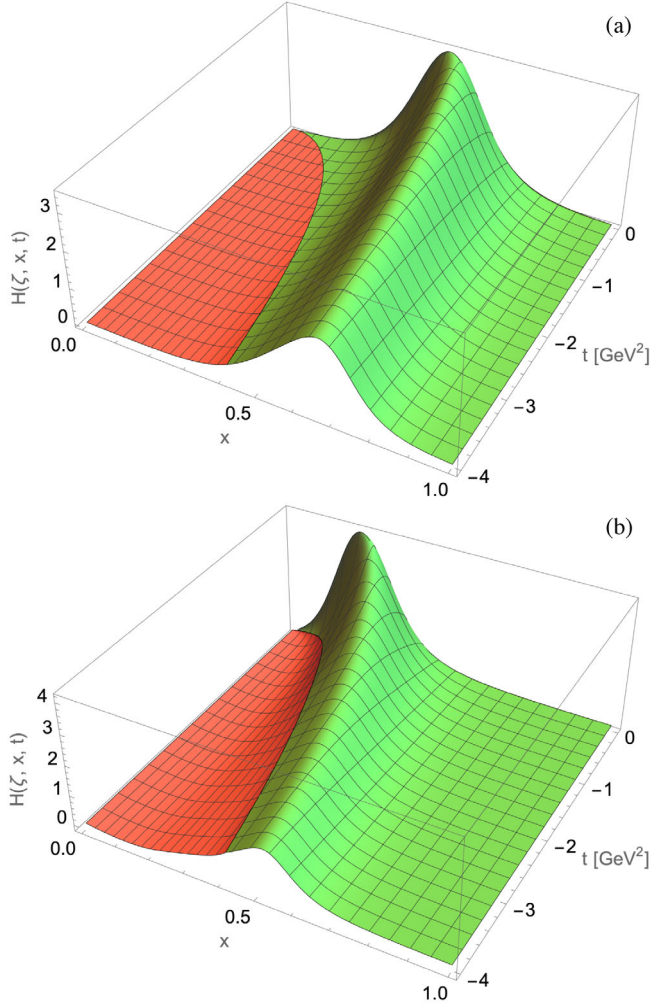Figure 9 shows the three-dimensional plots of $H(\zeta, x, t)$ for two parameter sets, $(m_{Q_1}, m_{Q_2}) = (2, 2)$ GeV and $(m_{Q_1}, m_{Q_2}) = (1, 3)$ GeV, whose results are presented in Figs. 9(a) and 9(b), respectively, in the range of $0 \le x \le 1$ and -4 GeV$^2 \le t \le 0$. The red and green regions correspond to GPDs in the ERBL $(0 \le x \le \zeta)$ and DGLAP $(\zeta \le x \le 1)$ regions, respectively. The crossover boundaries (black lines) between the two regions correspond to the lines $x = \zeta$, i.e., $H_{\mathrm{ERBL}}(\zeta, \zeta, t) = H_{\mathrm{DGLAP}}(\zeta, \zeta, t)$. Again t and ζ are not independent variables in $(1 + 1)$ dimensions. In the crossover boundary for a given parameter set, the longitudinal momentum fraction x carried by the struck constituent Q_1 gradually increases as $|t|$ increases. Also, the peak position of GPD always exists in the DGLAP region. Comparing the two parameter sets, the value of x at the peak is found to decrease as the mass ratio m_{Q_1}/m_{Q_2} decreases.

C. PDF and EM form factor

Figure 10 shows the ordinary valence PDF for the helium target multiplied by x, i.e., $xq_v(x)$ for three values of $m_{Q_1} = m_{Q_2}$ with $M_T = 3.7$ GeV. The dotted, solid, and dashed lines in this figure represent the results obtained with $m_{Q_{1(2)}} = 1.9$, 2.0, and 2.1 GeV, respectively. Since $q_v(x)$ in Eq. (38) is symmetric under the exchange of $x \to 1 - x$ for the case of equal constituent mass, $xq_v(x)$ is somehow asymmetric. In Fig. 10, this asymmetric behavior is getting noticeable as the binding gets stronger.

FIG. 9. Three-dimensional plots of $H(\zeta, x, t)$ for two parameter sets. (a) $(m_{Q_1}, m_{Q_2}) = (2, 2)$ GeV and (b) $(m_{Q_1}, m_{Q_2}) = (1, 3)$ GeV, in the region of $0 \le x \le 1$ and -4 GeV$^2 \le t \le 0$.

should be even larger to get $-t/Q^2 \lesssim 0.1$. Therefore, we find that the GPD handbag approximation can be valid only for a small value of $-t/Q^2$, although the critical value of $-t/Q^2$ appears somewhat larger as $-t$ increases in our $(1 + 1)$-dimensional results. This indicates that, for realistic VMP measurements in $(3 + 1)$ dimensions, a very forward scattering region should be required to invoke the GPD handbag approximation as the forward scattering region would allow a very small value of $-t$. Since $-t$ is not independent of the target mass M_T as shown in Eq. (4) in $(1 + 1)$ dimensions, the skewness parameter ζ gets smaller as M_T increases for a given $-t$ value. This indicates that the GPD handbag approximation agrees with the exact VMP result faster with a larger M_T than a smaller M_T, which appears to be the characteristic of the $(1 + 1)$-dimensional analysis.

As we have mentioned before, in $(1 + 1)$ dimensions, the GPD $H(\zeta, x, t)$ given by Eq. (33) is essentially a function of x and t since ζ and t are related to each other by Eq. (5).
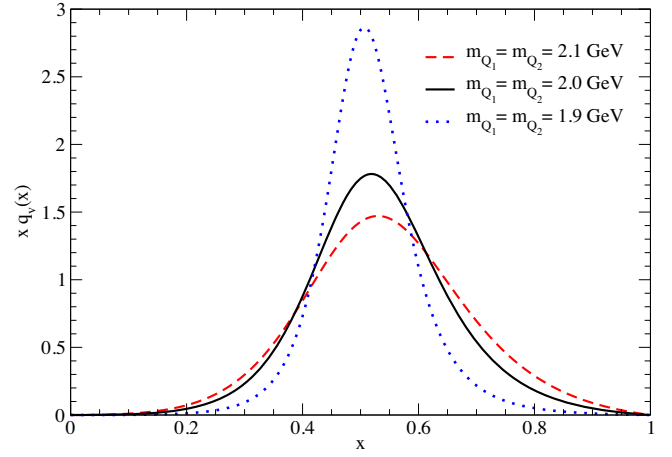
TABLE I. The nth moments $\langle y_n \rangle$ of the parton distribution function for the scalar target with three constituent mass sets.

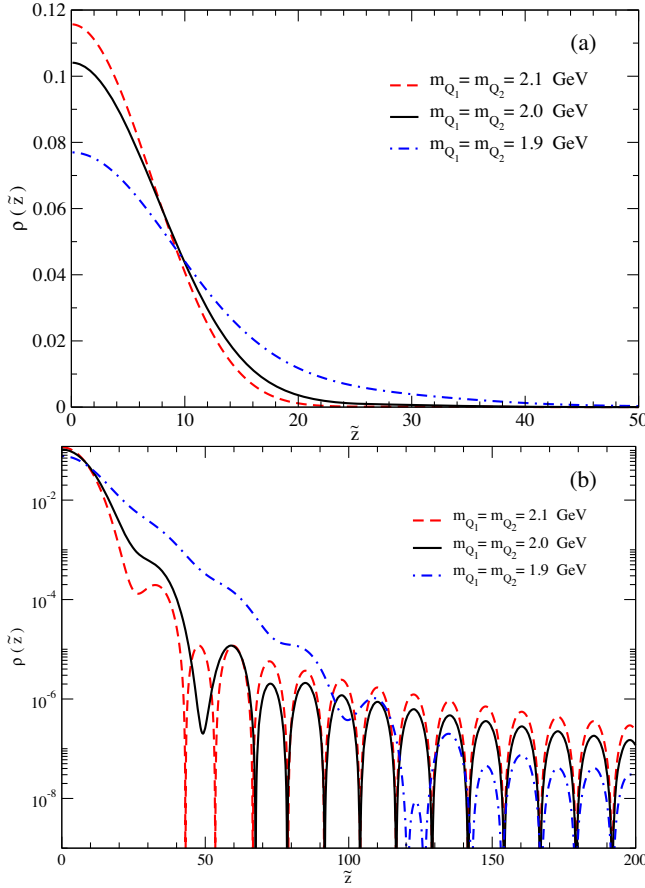| $m_{Q_1} = m_{Q_2}$	$\langle y_1 \rangle$	$\langle y_2 \rangle$	$\langle y_3 \rangle$	$\langle y_4 \rangle$	$\langle y_5 \rangle$	$\langle y_6 \rangle$
2.1 GeV	0	0.0884	0	0.0242	0	0.0104
2.0 GeV	0	0.0662	0	0.0155	0	0.0061
1.9 GeV	0	0.0313	0	0.0050	0	0.0016

FIG. 11. Longitudinal probability density $\varrho(\tilde{z})$ for the scalar target with $m_{Q_1} = m_{Q_2} = 1.9$, 2.0, and 2.1 GeV in the LF coordinate space $\tilde{z}$. (a) $\varrho(\tilde{z})$ in linear scale for the range of $0 \le \tilde{z} \le 50$, and (b) $\varrho(\tilde{z})$ in logarithmic scale in the range of $0 \le \tilde{z} \le 200$.

The nth moments of $q_v(x)$ for the scalar target are summarized in Table I. Since $q_v(y)$ in Eq. (40) is an even function of y, the odd-numbered moments vanish. Our results in Table I show that the heavier the constituent mass (or equivalently, the larger the binding energy) is, the greater are the values of the even-numbered moments. This implies that the shape of the PDF, $q_v(y)$, is more narrowly peaked at $y = 0$ and more suppressed at the end points ($y = \pm 1$) as the binding energy of the scalar target decreases.

Shown in Fig. 11 is the longitudinal probability density $\varrho(\tilde{z}) = |\psi(\tilde{z})|^2$ [see Eqs. (41) and (42)] for the scalar target with $M_T = 3.7$ GeV in the LF coordinate space of $\tilde{z} = x^- p^+$ which is completely Lorentz invariant in $(1 + 1)$ dimensions. The dot-dashed, solid, and dashed lines represent the results for $m_{Q_{1(2)}} = 1.9$, 2.0, and 2.1 GeV, respectively. In order to clearly show the behavior of the longitudinal probability density, we plot $\varrho(\tilde{z})$ in two ways. In Fig. 11(a), $\varrho(\tilde{z})$ is shown in the range of $0 \le \tilde{z} \le 50$ in linear scale. This shows that the more strongly bound state ($m_{Q_{1(2)}} = 2.1$ GeV) has a more concentrated distribution near $\tilde{z} = 0$ than weakly bound states have. The long-range
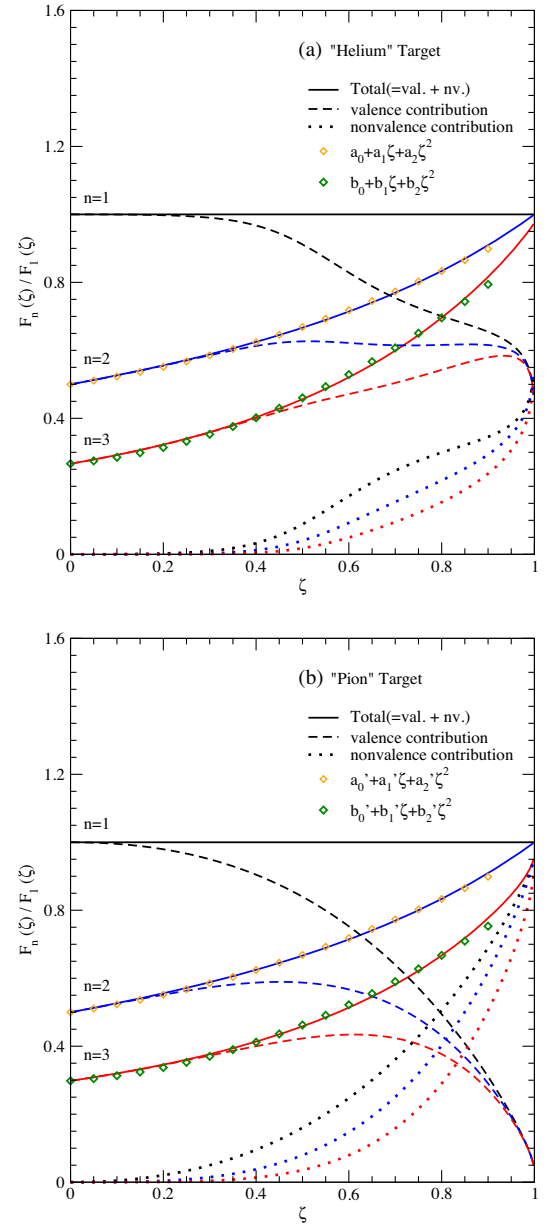

FIG. 12. The first three moments $\bar{F}_n(\zeta, t) \equiv \bar{F}_n(\zeta)$ ($n = 1, 2, 3$) of $H(\zeta, x, t)$ given by Eq. (43) for (a) the weakly bound helium target with $m_{Q_{1(2)}} = 2$ GeV and $M_T = 3.7$ GeV and (b) the strongly bound pion target with $m_{Q_{1(2)}} = 0.25$ GeV and $M_T = 0.14$ GeV, where $0 \le \zeta \le 1$ corresponds to $0 \le -t \le \infty$.

behavior of $\varrho(\tilde{z})$ is shown in Fig. 11(b) that plots the same function in logarithmic scale for a wider range of $\tilde{z}$. One can verify that $\varrho(\tilde{z})$ shows the oscillating behavior for large $\tilde{z}$. Furthermore, the onset of the oscillation appears earlier, and the amplitude of the oscillation is larger for the strongly bound states than the weakly bound states. Our observation is consistent with those for the pion case reported in Refs. [31,40,41].

We also investigate the dependence of our results on the value of the target mass M_T. In Fig. 12, we show the

first three moments $\bar{F}_n(\zeta, t) \equiv \bar{F}_n(\zeta) = F_n(\zeta)/F_1(\zeta)$ ($n = 1, 2, 3$) of GPD $H(\zeta, x, t)$ [see Eqs. (43)–(45)]. We consider a weakly bound state and a strongly bound state. Presented in Fig. 12(a) are the results for the weakly bound scalar target with $m_{Q_{1(2)}} = 2$ GeV and $M_T = 3.7$ GeV, which is dubbed the "helium" target. For comparison, we also show in Fig. 12(b) the results for the strongly bound scalar target with $m_{Q_{1(2)}} = 0.25$ GeV and $M_T = 0.14$ GeV, which is dubbed the "pion" target [23]. The black, blue, and red lines represent $\bar{F}_1(\zeta)$, $\bar{F}_2(\zeta)$, and $\bar{F}_3(\zeta)$, respectively. The dashed, dotted, and solid lines represent the valence contributions, the nonvalence contributions, and their sum, respectively. The valence and nonvalence contributions are obtained by replacing $H(\zeta, x, t)$ with $H_{DGLAP}(\zeta, x, t)$ and $H_{ERBL}(\zeta, x, t)$ in Eq. (33), respectively. The moments shown in Fig. 12 are indeed for the entire spacelike momentum transfer region since $0 \leq \zeta \leq 1$ corresponds to $0 \leq -t \leq \infty$.[5] In other words, the skewness parameter ζ is zero only at $t = 0$ and the nonvalence contributions always exist for nonzero skewness ($\zeta > 0$).

Our results presented in Fig. 12 give the following observations. (i) The first moments, $\bar{F}_1(\zeta)$, given by solid black lines are defined to be ζ independent while the sum rule for $n = 1$ yields the physical EM form factor. (ii) The redefined higher moments, $\bar{F}_2(\zeta)$ and $\bar{F}_3(\zeta)$, satisfy the polynomiality condition. In the figures, we plot the fitted $\bar{F}_2(\zeta)$ (orange diamonds) and $\bar{F}_3(\zeta)$ (green diamonds) by finding the corresponding polynomials up to the second order of ζ. (iii) The nonvalence contribution for the weakly bound helium target does not exceed the valence contribution for the entire momentum transfer region as shown in Fig. 12(a). However, the nonvalence contribution for the strongly bound pion is not negligible and indeed takes over the valence contribution at some points of ζ (or equivalently $-t$) as shown in Fig. 12(b). For example, the nonvalence contribution to the pion EM form factor ($n = 1$ case) is greater than the valence one for $\zeta \geq 0.8$ values.

Finally, we compute the EM form factor $F_{\mathcal{M}}(t)$ of the helium target as the first moment of $H(\zeta, x, t)$ for the spacelike $0 \leq -t < 40$ GeV^2 region, and the results are given in Fig. 13. The dashed, dotted, and solid lines represent the valence contributions, the nonvalence contributions, and their sums, respectively. In particular, we obtain the form factors by taking the plus (+) and minus (−) components of the current to examine the valence and nonvalence contributions in taking different components of the current while confirming that the sum of the valence and nonvalence contributions coincide whichever component is taken. Our results for $F_{\mathcal{M}}(t)$ shown in Fig. 13(a) are obtained by using Eqs. (31), (32), and (44) together with
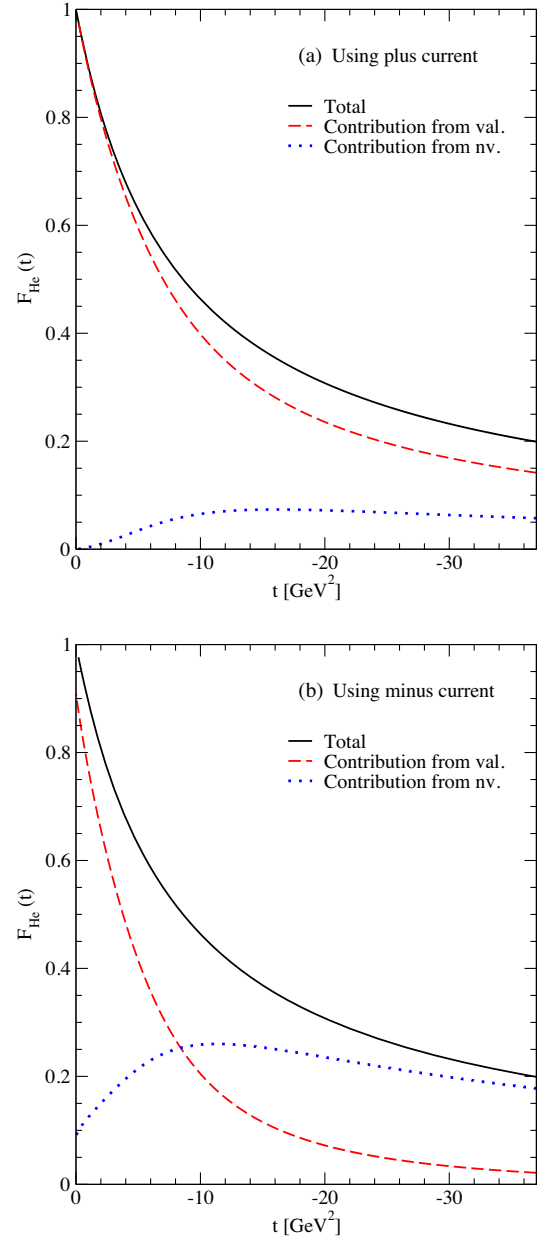

FIG. 13. Electromagnetic form factor $F_{\mathcal{M}}(t)$ of the helium target as the first moment of $H(\zeta, x, t)$ obtained for $m_{Q_{1(2)}} = 2$ GeV. The results are obtained by using (a) the plus current and (b) the minus current.

the "+" component of the current in the DVMP limit, which is exactly the same as our recent result reported in Ref. [23] based on the direct calculations of the triangle diagrams. Although one typically uses the + current to compute the form factor $F_{\mathcal{M}}(t)$, we compute here $F_{\mathcal{M}}(t)$ using the − component of the current as well in our direct triangle diagram calculation [23]. For comparison, we show in Fig. 13(b) the EM form factor obtained from the − component of the current using Eqs. (1) and (2) in Ref. [23]. All these results confirm that the total EM form factors are completely the same independent of the adopted

_____
[5]As we showed before, in $(1 + 1)$ dimensions, ζ and t are related to each other. But the relation depends on the mass. For example, $\zeta = 0.5$ corresponds to $-t = 6.85$ GeV^2 for the helium target but it corresponds to $-t = 0.01$ GeV^2 for the pion target.

component of the current and either the $+$ or $-$ component of the current can be used to obtain the EM form factor. However, the decomposition of the form factor depends on which component of the current is used for the calculation. This is apparent as shown in Figs. 13(a) and 13(b), where one can see that the nonvalence contribution is quite suppressed for the entire spacelike region when the $+$ current is used, while its contribution is not negligible but even exceeds the valence contribution for $|t| \gtrsim 8.5 \text{ GeV}^2$ when the $-$ current is used. Furthermore, the nonvalence contribution for the $-$ current case does not vanish even at $t = 0$ while it is zero for the $+$ current case. Therefore, the decomposition of the form factor as the valence and nonvalence contributions depends on which component of the current is used. It should be interpreted with great care noting which component of the current is used.

VI. SUMMARY AND CONCLUSION

In the present work, we investigated the light-front amplitudes of the virtual meson production process off the scalar target in $(1 + 1)$ dimensions using the scalar field model. Noting that there is only one CFF in $(1 + 1)$ dimensions for this process, we obtained the analytic expressions for all possible LF time-ordered amplitudes shown in Fig. 2. The obtained LF time-ordered amplitudes are individually boost invariant, and the sum of all LF time-ordered amplitudes turns out gauge invariant as they must be.

With the analytic solutions of the amplitudes at hand, we investigated various quantities, including the CFF, GPD, PDF, and EM form factor. We first tested the handbag dominance that has been adopted in the GPD formulation for the large Q^2 region. In particular, we explored the role of the cat's ears contributions, which have been typically ignored.

To quantify the individual contribution of the LF time-ordered amplitudes, we simulated the typical mass arrangement of the $\gamma^* + {}^4\text{He} \to f_0(980) + {}^4\text{He}$ process. Our numerical results showed that the gauge invariance is largely violated if one neglects the cat's ears contribution. In particular, the addition of the cat's ears contribution is crucial for the low Q^2 region. Although the violation appears smaller at $Q^2 > 10$–20 GeV^2 for the imaginary part of the total amplitude, it is still noticeable for the real part even at large Q^2 as shown in Fig. 5. This appears to limit the validity of the handbag dominance to the region of small $-t/Q^2$ [44]. Our numerical calculations in $(1 + 1)$ dimensions presented in Fig. 8 show that the handbag dominance appears limited to the kinematic region $-t/Q^2 \lesssim 0.1$ for its applicability both to the real and imaginary parts of the CFF. The relaxation of the condition $Q^2 \gg M_T^2$ in reaching the DVMP limit would also apply only for the forward production of the meson in $(3 + 1)$ dimensions. Therefore, the direct use of the handbag

dominance in the analyses of the proposed experiments at JLab [45], where such small values of $-t/Q^2$ are not reached, may be treacherous necessitating great care taking into account the higher order $-t/Q^2$ corrections not only from the kinematic higher twist contributions but also from the dynamic higher twist GPDs [16,46,47]. In this respect, the future Electron-Ion Collider project [48] is strongly called for the proper extraction of GPDs from the precision experimental data off the nucleon and nuclei targets focusing on the forward angle.

In our simple $(1 + 1)$-dimensional model computations, the limit $(\zeta, t) \to 0$ of the GPD, $H(0, x, 0) = H_{\text{DGLAP}}(0, x, 0)$, provides the PDF, $q_v(x)$, which could be interpreted as the probability of finding the constituent inside the hadron as a function of the momentum fraction x carried by the constituent. It is equivalent to the square of the LF wave function, i.e., $q_v(x) = |\psi(x)|^2$. In $(1 + 1)$ dimensions, the LF spatial variable $\tilde{z} = x^- p^+$ is completely Lorentz invariant providing an intrinsic longitudinal probability density $\varrho(\tilde{z})$. Our numerical results showed that the more strongly bound state concentrates the density more at $\tilde{z} = 0$ than the less strongly bound states do, which appears to be consistent with the intuitive understanding of the bound-state system. The polynomiality condition for the moments of GPD appears also well satisfied. The GPD sum rule provided the EM form factor $F_{\mathcal{M}}(t)$ confirming the valence and nonvalence contributions that we obtained previously [23], which corresponded to the GPD contributions from the DGLAP and ERBL regions, respectively.

In the calculation of the electromagnetic properties of hadrons in the LF formulation, one may use not only the plus $(+)$ component but also any other component of the current as they are supposed to give the identical results. As shown in Fig. 13, we indeed confirmed that the two components $(+$ or $-)$ led to the identical form factor. However, the decomposition of the form factor into valence and nonvalence contributions appears quite different depending on the component of the current used in the extraction. This indicates that it requires great care in interpreting the valence and nonvalence contributions to the form factor.

Our $(1 + 1)$-dimensional analyses performed in the present work would be extended to the more realistic $(3 + 1)$-dimensional analyses, where the contributions from the transverse component of the current would be important. In particular, the two CFFs $\mathcal{F}_1$ and $\mathcal{F}_2$ involved in the scalar meson production off the scalar target are independent of each other in $(3 + 1)$ dimensions. Thus, the investigation of the beam spin asymmetry proportional to $\mathcal{F}_1 \mathcal{F}_2^* - \mathcal{F}_2 \mathcal{F}_1^*$ for this process would provide a unique opportunity not only to explore the imaginary part of the hadronic amplitude in our general formulation but also to examine the significance of the chiral-odd GPD contribution in the leading-twist GPD formulation. The work along this line of thought is currently under way.

[1] R. Hofstadter and R. W. McAllister, Electron scattering from the proton, Phys. Rev. **98**, 217 (1955).

[2] M. Breidenbach, J. I. Friedman, H. W. Kendall, E. D. Bloom, D. H. Coward, H. DeStaebler, J. Drees, L. W. Mo, and R. E. Taylor, Observed Behavior of Highly Inelastic Electron-Proton Scattering, Phys. Rev. Lett. **23**, 935 (1969).

[3] J. Ashman *et al.* (European Muon Collaboration), An investigation of the spin structure of the proton in deep inelastic scattering of polarized muons on polarized protons, Nucl. Phys. **B328**, 1 (1989).

[4] X. Ji, Gauge-Invariant Decomposition of Nucleon Spin, Phys. Rev. Lett. **78**, 610 (1997).

[5] X. Ji, Deeply-virtual Compton scattering, Phys. Rev. D **55**, 7114 (1997).

[6] A. V. Radyushkin, Scaling limit of deeply virtual Compton scattering, Phys. Lett. B **380**, 417 (1996).

[7] A. V. Radyushkin, Nonforward parton distributions, Phys. Rev. D **56**, 5524 (1997).

[8] D. Müller, D. Robaschik, B. Geyer, F.-M. Dittes, and J. Hořejši, Wave functions, evolution equations and evolution kernels from light-ray operators of QCD, Fortschr. Phys. **42**, 101 (1994).

[9] K. Goeke, M. V. Polyakov, and M. Vanderhaeghen, Hard exclusive reactions and the structure of hadrons, Prog. Part. Nucl. Phys. **47**, 401 (2001).

[10] M. Diehl, Generalized parton distributions, Phys. Rep. **388**, 41 (2003).

[11] A. V. Belitsky and A. V. Radyushkin, Unraveling hadron structure with generalized parton distributions, Phys. Rep. **418**, 1 (2005).

[12] H.-M. Choi, C.-R. Ji, and L. S. Kisslinger, Skewed quark distribution of the pion in the light-front quark model, Phys. Rev. D **64**, 093006 (2001); Continuity of generalized parton distributions for the pion virtual Compton scattering, Phys. Rev. D **66**, 053011 (2002).

[13] L. Favart, M. Guidal, T. Horn, and P. Kroll, Deeply virtual meson production on the nucleon, Eur. Phys. J. A **52**, 158 (2016).

[14] R. Tarrach, Invariant amplitudes for virtual Compton scattering off polarized nucleons free from kinematical singularities, zeros and constraints, Nuovo Cimento Soc. Ital. Fis. **28A**, 409 (1975).

[15] A. Metz, Virtuelle Comptonstreuung und die Polarisierbarkeiten des Nukleons (in German), Ph.D. thesis, University Mainz, 1997.

[16] A. V. Belitsky and D. Müller, Refined analysis of photon leptoproduction off a spinless target, Phys. Rev. D **79**, 014017 (2009).

[17] K. Kumerički and D. Müller, Deeply virtual Compton scattering at small x_B and the access to the GPD H, Nucl. Phys. **B841**, 1 (2010).

[18] B. L. G. Bakker and C.-R. Ji, A study of Compton form factors in scalar QED, Few-Body Syst. **55**, 395 (2014).

[19] H. Bethe and W. Heitler, On the stopping of fast particles and on the creation of positive electrons, Proc. R. Soc. A **146**, 83 (1934).

[20] M. Hattawy *et al.* (CLAS Collaboration), First Exclusive Measurement of Deeply Virtual Compton Scattering off ^{4}He: Toward the 3D Tomography of Nuclei, Phys. Rev. Lett. **119**, 202004 (2017).

[21] C.-R. Ji, H.-M. Choi, A. Lundeen, and B. L. G. Bakker, Beam spin asymmetry in electroproduction of pseudoscalar or scalar meson production off the scalar target, Phys. Rev. D **99**, 116008 (2019).

[22] G. C. Wick, Properties of Bethe-Salpeter wave functions, Phys. Rev. **96**, 1124 (1954); R. E. Cutkosky, Solutions of a Bethe-Salpeter equation, Phys. Rev. **96**, 1135 (1954).

[23] Y. Choi, H.-M. Choi, C.-R. Ji, and Y. Oh, Light-front dynamic analysis of the longitudinal charge density using the solvable scalar field model in $(1 + 1)$ dimensions, Phys. Rev. D **103**, 076002 (2021).

[24] M. Sawicki and L. Mankiewicz, Solvable light-front model of a relativistic bound state in $1 + 1$ dimensions, Phys. Rev. D **37**, 421 (1988).

[25] L. Mankiewicz and M. Sawicki, Solvable light-front model of the electromagnetic form factor of the relativistic two-body bound state in $1 + 1$ dimensions, Phys. Rev. D **40**, 3415 (1989).

[26] M. Sawicki, Light-front limit in a rest frame, Phys. Rev. D **44**, 433 (1991); Soft charge form factor of the pion, Phys. Rev. D **46**, 474 (1992).

[27] St. Głazek and M. Sawicki, Relativistic bound-state form factors in a solvable $(1 + 1)$-dimensional model including pair creation, Phys. Rev. D **41**, 2563 (1990).

[28] S. J. Brodsky and D. S. Hwang, Exact light-cone wave-function representation of matrix elements of electroweak currents, Nucl. Phys. **B543**, 239 (1998).

[29] H.-M. Choi and C.-R. Ji, Nonvanishing zero modes in the light-front current, Phys. Rev. D **58**, 071901 (1998).

[30] N. C. J. Schoonderwoerd and B. L. G. Bakker, Equivalence of renormalized covariant and light-front perturbation theory. I. Longitudinal divergences in the Yukawa model, Phys. Rev. D **57,** 4965 (1998); Equivalence of renormalized covariant and light-front perturbation theory. II. Transverse divergences in the Yukawa model, Phys. Rev. D **58,** 025013 (1998).

[31] G. A. Miller and S. J. Brodsky, Frame-independent spatial coordinate $\tilde{z}$: Implications for light-front wave functions, deep inelastic scattering, light-front holography, and lattice QCD calculations, Phys. Rev. C **102,** 022201(R) (2020).

[32] V. N. Gribov and L. N. Lipatov, Deep inelastic ep scattering in perturbation theory, Sov. J. Nucl. Phys. **15,** 438 (1972).

[33] Y. L. Dokshitzer, Calculation of the structure functions for deep inelastic scattering and e^+e^- annihilation by perturbation theory in quantum chromodynamics, Sov. J. Nucl. Phys. **46,** 641 (1977).

[34] G. Altarelli and G. Parisi, Asymptotic freedom in parton language, Nucl. Phys. **B126,** 298 (1977).

[35] A. V. Efremov and A. V. Radyushkin, Factorization and asymptotic behaviour of pion form factor in QCD, Phys. Lett. **94B,** 245 (1980).

[36] G. P. Lepage and S. J. Brodsky, Exclusive processes in quantum chromodynamics: Evolution equations for hadronic wavefunctions and the form factors of mesons, Phys. Lett. **87B,** 359 (1979).

[37] G. P. Lepage and S. J. Brodsky, Exclusive processes in perturbative quantum chromodynamics, Phys. Rev. D **22,** 2157 (1980).

[38] J. C. Collins, L. Frankfurt, and M. Strikman, Factorization for hard exclusive electroproduction of mesons in QCD, Phys. Rev. D **56,** 2982 (1997).

[39] V. L. Chernyak and A. R. Zhitnitsky, Asymptotic behaviour of exclusive processes in QCD, Phys. Rep. **112,** 173 (1984).

[40] S. J. Brodsky and G. F. de Téramond, Light-front dynamics and AdS/QCD correspondence: The pion form factor in the space- and time-like regions, Phys. Rev. D **77,** 056007 (2008).

[41] G. F. de Téramond, T. Liu, R. S. Sufian, H. G. Dosch, S. J. Brodsky, and A. Deur (HLFHS Collaboration), Universality of Generalized Parton Distributions in Light-Front Holographic QCD, Phys. Rev. Lett. **120,** 182001 (2018).

[42] X. Ji, W. Melnitchouk, and X. Song, Study of off-forward parton distributions, Phys. Rev. D **56,** 5511 (1997).

[43] A. V. Radyushkin, Symmetries and structure of skewed and double distributions, Phys. Lett. B **449,** 81 (1999).

[44] C.-R. Ji and B. L. G. Bakker, Conceptual issues concerning generalized parton distributions, Int. J. Mod. Phys. E **22,** 1330002 (2013); B. L. G. Bakker and C.-R. Ji, Spin filter in deeply virtual Compton scattering amplitudes, Phys. Rev. D **83,** 091502(R) (2011).

[45] J. Roche *et al.*, Measurements of the electron-helicity dependent cross sections of deeply virtual Compton scattering with CEBAF at 12 GeV, arXiv:nucl-ex/0609015.

[46] A. V. Belitsky, D. Müller, A. Kirchner, and A. Schäfer, Twist-three analysis of photon electroproduction off the pion, Phys. Rev. D **64,** 116002 (2001).

[47] V. M. Braun, A. N. Manashov, and B. Pirnay, Finite-t and target mass corrections to deeply virtual Compton scattering on a scalar target, Phys. Rev. D **86,** 014003 (2012).

[48] R. Abdul Khalek *et al.*, Science requirements and detector concepts for the electron-ion collider: EIC yellow report, arXiv:2103.05419.